Mathematical modelling of the mechanical response of geosynthetic-reinforced and pile-supported embankments

Received: 11 July 2022 | Revised: 31 May 2023 | Accepted: 3 June 2023

DOI: 10.1002/nag.3586

RESEARCH ARTICLE

WILEY

Mathematical modelling of the mechanical response of geosynthetic-reinforced and pile-supported embankments

Viviana Mangraviti[1,2] | **Luca Flessati**[2,3] | **Claudio di Prisco**[2]

[1]Department of Architecture and Civil Engineering, Chalmers University of Technology, Goteborg, Sweden

[2]Department of Civil and Environmental Engineering, Politecnico di Milano, Milan, Italy

[3]Faculty of Civil Engineering and Geoscience, Delft University of Technology, Delft, Netherlands

Correspondence
Viviana Mangraviti, Department of Architecture and Civil Engineering, Chalmers University of Technology, SE-412 96 Gothenburg, Sweden.
Email: viviana.mangraviti@chalmers.se

Abstract

Piled foundations are commonly employed to reduce settlements in artificial earth embankments founded on soft soil strata. To limit the number of piles and, consequently, construction costs, popular is the use of geosynthetic reinforcements laid at the embankment base. Nowadays, the complex interaction between geosynthetics, piles and soil is not yet fully understood and, in the scientific literature, simplified displacement-based approaches to choose reinforcements, pile diameter and spacing are missing. In this paper, the authors, starting from the critical analysis and theoretical interpretation of finite difference numerical results, introduce a new mathematical model to rapidly assess both (i) differential/average settlements at the top of the embankment and (ii) maximum tensile forces in the basal reinforcement. The model, conceived to reproduce the response of a pile belonging to the central part of the embankment, is the result of an upscaling procedure based on a suitable sub-structuring of the spatial domain (an axisymmetric unit cell) and on the concept of plane of equal settlements. For the foundation soil, drained conditions are considered, the pile skin roughness is disregarded, and piles are assumed to get the rigid bedrock. As generalised kinematic variables average and differential settlements are employed, whereas as generalized static ones the embankment height and the geosynthetic axial force. The model is validated against field measurements (where layered foundation soil and pile caps are included) and an application example of the model, used as a preliminary design tool in a displacement-based perspective, is finally provided.

KEYWORDS

displacement-based design, geosynthetic-reinforced pile-supported embankments, preliminary design, geosynthetic reinforcement, geosynthetic maximum tensile force, simplified method

1 | INTRODUCTION

A very popular strategy to reduce settlements of artificial earth embankments founded on soft soil strata consists in employing regularly spaced piles. To improve the pile effectiveness, the use of geosynthetic reinforcements, laid at the embankment base, is very common. In the past three decades, several researchers have tried to better understand the interaction mechanisms developing in Geosynthetic-Reinforced Pile-Supported (GRPS) embankments, being aware of the necessity of improving the available design methods of these complex "geo-structures" (composed of piles, reinforcement, embankment and foundation soil).

According to the current state of the art, the mechanical behaviour of both Conventional Pile-Supported (CPS, i.e., piled embankments without basal geosynthetic reinforcements) and GRPS embankments is mainly governed by (i) the "arching effect" within the embankment body, that is the stress transfer mechanism towards the piles and (ii) the arising of the plane of equal settlements within the embankment, that is the plane above which differential settlement increments are negligible.

As was experimentally shown by many authors by performing small-scale centrifuge model tests,[1–6] trapdoor tests,[7–10] and full-scale field tests,[11–25] the arching effect depends on both geometrical and mechanical properties of the elements composing the geo-structure. The experimental results also put in evidence that the stresses acting on the foundation soil are significantly affected by the differential displacements experimentally imposed at the base, suggesting the system response to be mainly governed by the material deformability.

The mechanical response of GRPS embankments was also studied numerically by performing non-linear either Finite Element (FE) or Finite Difference (FD) numerical analyses. Due to the complexity of the problem (its geometry is three-dimensional and geosynthetics behave like membranes under large displacements), even nowadays, numerical analyses are not usually employed in the pre-design phase. The objective of this paper is to introduce an upscaled model, significantly reducing computational time (the model requires few seconds to run), to be used as a pre-design tool for GRPS embankments.

In the design of these complex geo-structures, two are the problems to be solved: the lateral spreading of foundation soil placed under the embankment flanks and the average/differential settlements developing in the central part of the embankment.

In the past, many authors have disregarded the role of large displacements[21,26–34] only very recently Mangraviti et al.[35] took into consideration the large-displacement membranal behaviour of reinforcements.

In this paper, the main focus is on the average/differential settlements developing in the central part of the embankment and, as was already suggested by many authors,[26,36–44] the unit cell approach is followed.

In practical applications, CPS and GRPS embankments are commonly designed by using models based on the unit cell approach. These, according to van Eekelen et al.,[45] may be classified as (i) rigid arch models, (ii) equilibrium models, and (iii) frictional models. In the models belonging to the first category,[46–50] materials mechanical properties are disregarded and the stress redistribution is assumed to depend only on system geometry. According to the equilibrium models,[45,51–54] an ideal stress arch is assumed to develop within the embankment and vertical stresses are redistributed by imposing the balance of momentum of the arch.

Other authors, by using the limit equilibrium method and by assuming a frictional rigid-perfectly plastic constitutive relationship[55–61] for the soil, introduced models accounting for both geometry and embankment soil shear strength properties.

All the previously cited models disregard the deformability of the various elements constituting the system, that are embankment, foundation soil and geosynthetic reinforcement (the deformability of the latter is accounted for only in van Eekelen et al.[45]), and cannot be employed in a displacement-based design perspective. In contrast, according to the authors and as was stated by King et al.,[62] to ensure the serviceability of the embankment over its all lifetime, the design of GRPS embankments has to be based on the assessment of average and differential settlements.

As was previously mentioned, the attempts of introducing a simplified numerical model dealing with both stresses and settlements are very few. For instance, although with reference to the classical trapdoor problem, Filz and Smith[63] and Filz et al.[64,65] proposed a model putting in relation vertical stress transfer to differential displacements at the embankment base. Very recently, di Prisco et al.[40] proposed a generalised constitutive relationship to evaluate, under drained conditions, both differential and average settlements at the top of the unit cell caused by CPS embankment construction. This constitutive relationship, derived by the interpretation of the results of a series of FD numerical analyses, was conceived by following a substructuring approach and an upscaling procedure. The constitutive law can be employed to pre-design geometry (pile diameter and spacing) and compute the costs, once the system performance (e.g., displacements at the embankment top) is assigned.[66]

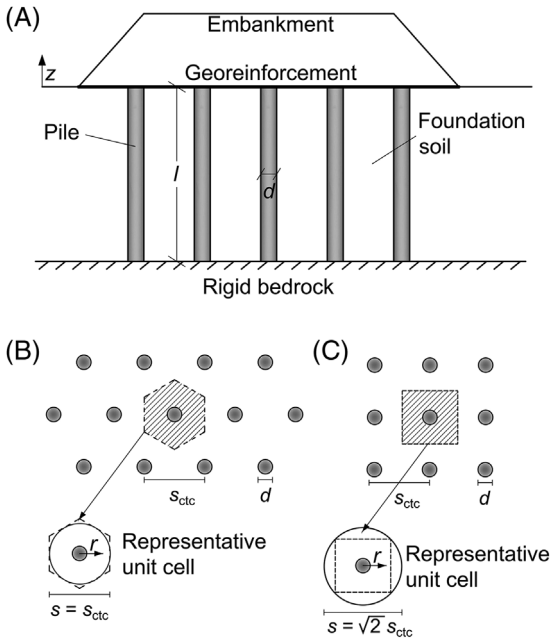

FIGURE 1 GRPS embankment: (A) problem geometry. Representative unit cell for both (B) triangular and (C) square piles pattern according to McGuire.[61]

In this paper the same approach used by di Prisco et al.[40] for CPS embankments is used to define a new upscaled constitutive relationship for GRPS embankments by considering large-displacements finite difference numerical analyses results (implemented in FLAC3D 6.0[67]) by Mangraviti et al.[35] The new model can be used to optimise the design of both piles and geosynthetic reinforcement with the aim of increasing the sustainability of GRPS embankments.[68]

The problem analysed in this paper is ideal: the pile shaft is assumed to be smooth, the piles to be founded on a rigid bedrock and the embankment construction to take place under drained conditions. However, since the model is based on a substructuring of the spatial domain, it can be extended to the case of floating piles, hydromechanical coupling and rough pile shafts.[43]

The paper is structured as it follows: for the sake of clarity in Section 2 the main numerical evidences from Mangraviti et al.[35] are summarised, giving an interpretation of the mechanical behaviour of GRPS embankments; in Section 3 the new constitutive model for GRPS embankments is illustrated; in Section 4 the model is verified against the numerical results from Mangraviti et al.[35] and in Section 5 it is validated against field measurements. Finally, in Section 6 a practical application of the constitutive model is presented.

2 | NUMERICAL EVIDENCE FOR GRPS EMBANKMENTS

For the sake of clarity, hereafter, the mechanical response of GRPS embankments is described in the light of the numerical results obtained by Mangraviti et al.,[35] where the problem schematised in Figure 1(A) was considered and the effects of the layer-by-layer embankment construction under drained conditions of GRPS embankments studied in detail. In agreement with what already suggested in the literature,[26,36–38,40,43,69,70] the authors reduced the problem to the analysis of one axisymmetric cell, considered as representative for the central part of the embankment. The diameter s of the equivalent unit cell can be calculated as in McGuire[61] to account for the piles pattern (e.g., the cases of both triangular and square piles disposition are reported in Figure 1B, C).

The axisymmetric unit cell includes: (i) the embankment, whose height h evolves during the layer-by-layer construction process, (ii) the geosynthetic reinforcement laid at the embankment base, (iii) one pile of diameter d and length l, (iv) a homogeneous soft soil stratum of thickness l and (v) a rigid bedrock. In agreement with what done by other authors, the large-displacements numerical analyses were performed by assuming an elastic-perfectly plastic constitutive relationship for the soil[29,32,34,36,61,71–73] whereas an elastic behaviour for both pile and reinforcement.[27,34,63,74] This latter is assumed to behave as an isotropic membrane[27,34,63,74] with nil flexural stiffness.

TABLE 1 Geometry for one reference case from Mangraviti et al.[35]

d (m)	s (m)	l (m)
0.5	1.5	5

TABLE 2 Mechanical properties for one reference case from Mangraviti et al.[35]

	Unit weight (kN/m^3)	Young's modulus (MPa)	Poisson ratio (–)	Friction angle (°)	Cohesion (kPa)	Dilatancy angle (°)	J (kN/m)
Foundation soil	18	1	0.3	30	0	0	–
Embankment	18	10	0.3	40	0	0	–
Pile	25	30000	0.3	–	–	–	–
Geosynthetic reinforcement	–	–	0.3	–	–	–	1000

Since geosynthetics are very often anisotropic (their stiffness/strength is different depending on the loading direction), the values of stiffness/strength to be assigned to the equivalent isotropic membrane are the average ones. A discussion on this strategy is reported in Boschi et al.[75]

The interface between piles and soil was assumed to be smooth, whereas a frictional interface was considered between reinforcement and soil.

During the embankment construction, Mangraviti et al.[35] have shown that, due to the difference in stiffness between pile and foundation soil, differential displacements accumulate at the embankment base. Consequently, (i) strains localise in the proximity of the pile edge (defining the "process height", see Section 2.1), (ii) stresses tend to migrate towards the piles ("arching effect", in Section 2.2) and the geosynthetic reinforcement is progressively loaded (membranal effect, in Section 2.3). With the aim of introducing the upscaled constitutive relationship for the system (in Section 3), the substructuring of the spatial domain outlined in Mangraviti et al.[35] is reported and discussed in Section 2.4, whereas in Section 2.5 the modelling of the mechanical behaviour of each sub-structure is introduced in the light of the numerical results.

For the sake of brevity, the results from Mangraviti et al.[35] discussed in the following will be reported only for one representative reference case, whose geometry and mechanical properties are listed in Tables 1 and 2, respectively, where J is the tensile axial stiffness of the geosynthetic reinforcement.

2.1 | Process height

As was previously mentioned, during the embankment construction, due to the difference in stiffness between pile and foundation soil, differential settlements accumulate at the base of the embankment and shear strains localise in a cylindrical narrow crown close to the pile edge, defined as "process zone". As described in Mangraviti et al.,[35] the height of the "process zone", h_p, is initially equal to the embankment height and, when the embankment height becomes sufficiently large, the arching effect is "mature" and h_p stops evolving ($h = h_p = h_r^*$, Figure 2A). A schematic geometrical representation for h_p when $h > h_r^*$ is given in Section 2.4 (Figure 8). The geometrical and mechanical properties of the reference case are listed in the Figure 2(A), where: E_e, ϕ'_e and ψ_e are the Young's modulus, the friction angle and the dilatancy angle of the embankment soil, respectively; E_f, and ϕ'_f the Young's modulus and the friction angle of the foundation soil, respectively.

Until $h < h_r^*$, differential settlements develop at the embankment top, whereas for $h > h_r^*$ they are nil.[35] This implies that, for $h > h_r^*$, $z = h_r^*$ (vertical coordinate z defined in Figure 1A) represents the height of the plane of equal settlements.

Mangraviti et al.[35] have shown that h_r^* does not only depend on the geometry and material properties, but also on the reinforcement tensile axial stiffness (Figure 2B).

2.2 | Arching effect

In Figure 3(A), the numerical results for the reference case are plotted in terms of contour of vertical stresses (σ_v) for $h = 5$ m and for $d/2 < r < s/2$ (coordinate r defined in Figure 1B, C) and $0 < z < h_r^*$. Due to the arching effect, vertical stresses are not uniform in the embankment and, in particular, at $z = 0$ (solid line of Figure 3B), for $r/d = 1/2$ vertical

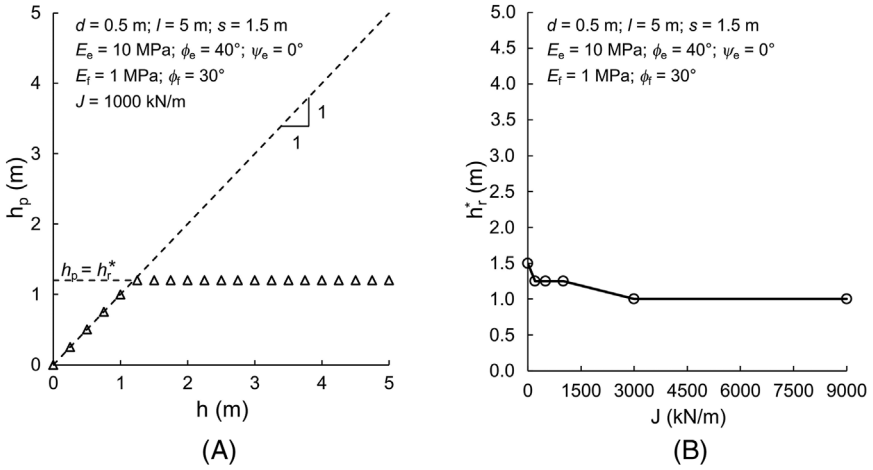

FIGURE 2 Numerical results for one reference case from Mangraviti et al.[35] in terms of: (A) evolution of h_p during construction and (B) influence of J on h_r^* in GRPS embankments.

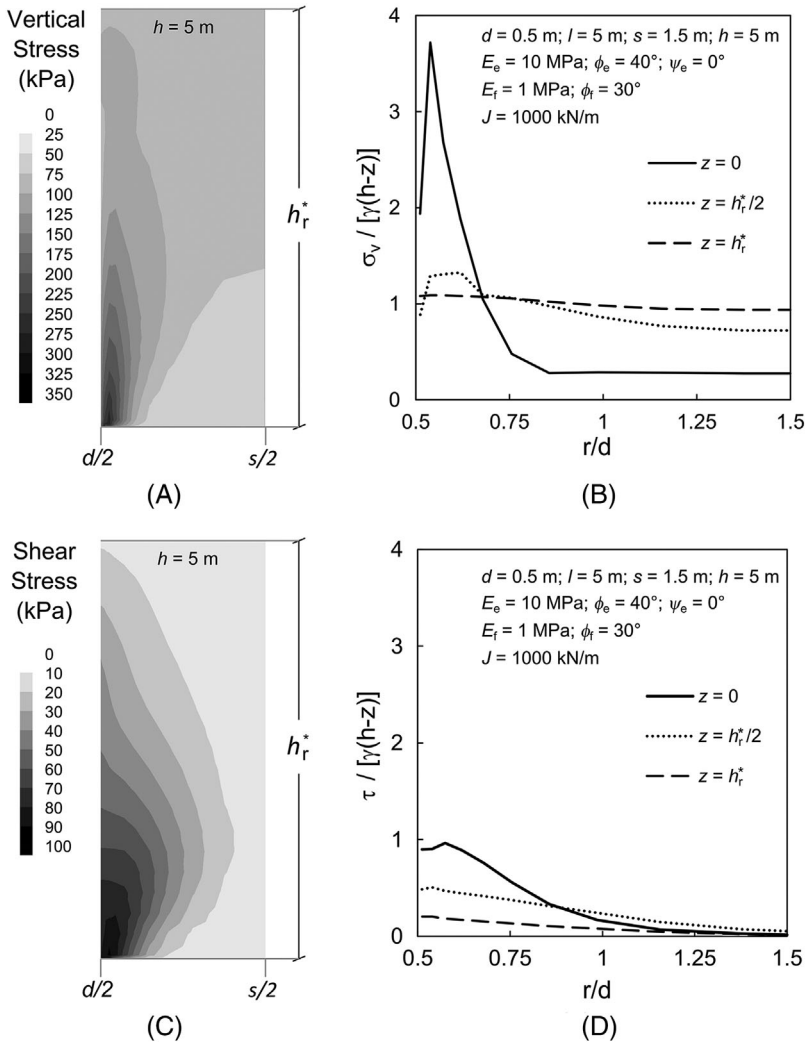

FIGURE 3 Numerical results for one reference case from Mangraviti et al.[35] in terms of (A) vertical stress contour plot; (B) normalised vertical stress profiles along the radial coordinate; (C) shear stress contour plot; (D) normalised shear stress profiles along the radial coordinate within the process zone of the embankment above the soft soil, that is, between $d/2 < r < s/2$ and $0 < z < h_r^* = 1.1\ m$.

stresses are significantly larger than the ones corresponding to $r/d = s/(2d) = 1.5$. This difference markedly decreases for larger z values (dotted line of Figure 3B) and nullifies for $z = h_r^*$ (dashed line in Figure 3B), where vertical stresses are practically coincident with the geostatic ones ($\sigma_v/[\gamma(h-z)] = 1$, being γ the embankment soil unit weight).

The vertical stress redistribution towards the piles is associated with the development of shear stresses, τ, (Figure 3C, representing the contour plot of τ for $d/2 < r < s/2$ and $0 < z < h_r^*$), whose maximum value is obtained for $r = d/2$. The distribution of $\tau/[\gamma(h-z)]$ along r/d for $z = 0$, $h_r^*/2$ and h_r^* are illustrated in Figure 3D. Even if at $z = h_r^*$ vertical stresses

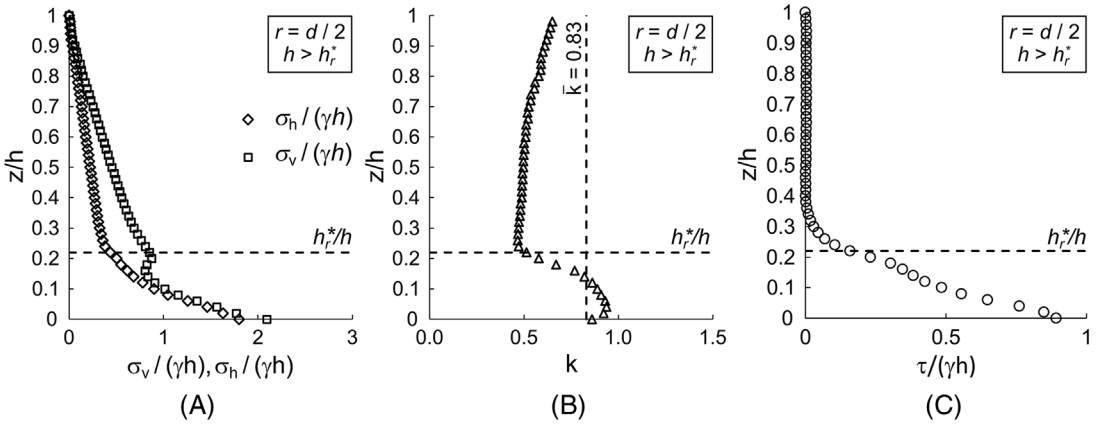

FIGURE 4 Numerical results for the reference case from Mangraviti et al.[35] (Tables 1 and 2) in terms of distribution of normalised (A) vertical and horizontal stress; (B) k ratio and (C) tangential stresses along the embankment for $r = d/2$ and $h = 5\ m > h_r^* = 1.1\ m$ (Figure 2).

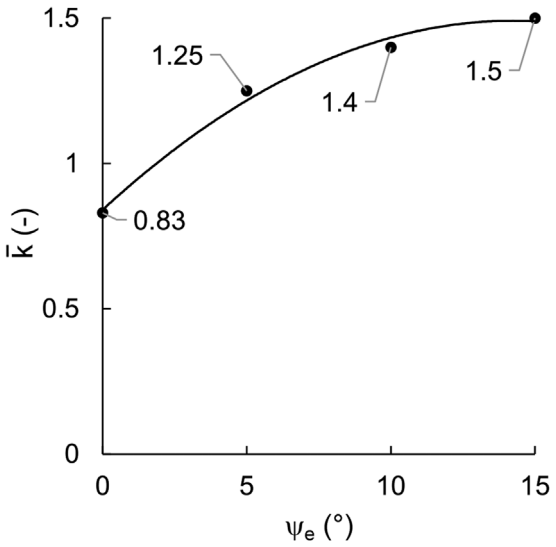

FIGURE 5 Numerical results for GRPS embankments in terms of evolution of $\bar{k}$ with ψ_e.

are almost uniform, shear stresses are not nil, but their value is negligible with respect to vertical stresses (dashed lines in Figure 3B).

To further put in evidence the development of the arching effect, the distributions along z of normalised σ_v and σ_h (horizontal stresses); $k = \sigma_h/\sigma_v$ and normalised τ for $r = d/2$ are plotted in Figure 4(A–C), respectively. For $z/h > h_r^*/h$, the σ_v and σ_h distributions are linear and practically coincident with the geostatic ones and τ are practically negligible. For z/h slightly larger than h_p/h (in Figure 4 the particular case of $h > h_r^*$ is represented, so that $h_p/h = h_r^*/h$), τ starts increasing due to the previously mentioned localisation of shear strains taking place in the process zone. For $0 < z/h < h_r^*/h$: (i) σ_v and σ_h stop increasing linearly along depth (Figure 4A), (ii) k starts increasing (Figure 4B) and (iii) τ severely increase (Figure 4C).

The distribution of k is affected by J, ψ_e , and ϕ_e', but its average value ($\bar{k}$) is practically unaffected by both J and ϕ_e'. The dependency of $\bar{k}$ on ψ_e (Figure 5) is coincident with the one numerically obtained for CPS embankments in di Prisco et al.[40] For $\psi_e = 0$, $\bar{k} = 0.83$ value practically coincides with the one experimentally obtained by Da Silva Burke and Elshafie.[76]

2.3 | Membranal mechanical response of geosynthetic reinforcement

The stress distribution acting on the membrane (solid line of Figure 6A) is characterised by a well-pronounced peak and significantly differs from the one assumed by both British and German current design standards,[77,78] but it is similar to

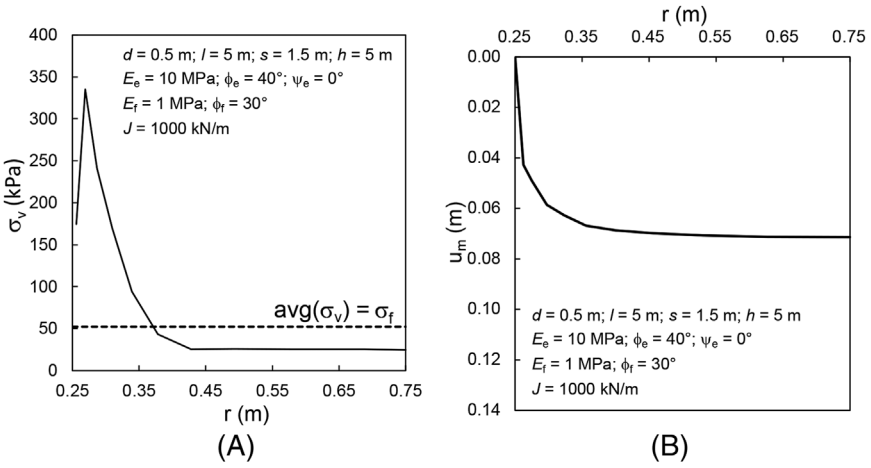

FIGURE 6 Numerical results for the reference case from Mangraviti et al.[35] in terms of (A) vertical stress acting above the membrane ($z = 0$) and (B) vertical displacement of the geosynthetic reinforcement along r for $h = 5$ m.

the one proposed by the Dutch current one.[79] The vertical displacement of the membrane ($u_m = u\ (r,\ z = 0)$, being u the vertical displacement at the base of the embankment), is coincident with the one of the top of the foundation soil and is not parabolic along r (Figure 6B), as it would be expected in case of uniform pressure (as assumed by the British Standards[77]). In fact, for $r > 0.4\ m$, u_{m} is practically constant, which means that the membrane is undeformed.

Tensile forces acting in the membrane $T(r)$, obtained by integrating tensile stresses along the infinitesimal circular crown at the distance r from the origin, evolve during construction. The maximum tensile force, obtained at the pile edge ($T_{max} = T(r = d/2)$) is plotted in Figure 7 against the average settlements at the bottom of the embankment, $u_{b,f}$. In Figure 7, the dependence of T_{max} on $u_{b,f}$ is satisfactorily interpolated by a quadratic function that will be used in the following for the upscaled constitutive model (see Section 3.2).

2.4 | Substructuring approach

From a detailed analysis of numerical results, Mangraviti et al.[35] have individuated six subdomains within the unit cell representing GRPS embankments (Figure 8). In particular, subdomain number: (1) is the pile; (2) is the foundation soil; (3) is the embankment for $0 < r < d/2$ and $0 < z < h_p$; (4) is the embankment for $d/2 < r < s/2$ and $0 < z < h_p$; (5) is the embankment for $0 < r < d/2$ and $h_p < z < h$; (6) is the embankment for $d/2 < r < s/2$ and $h_p < z < h$. The height of

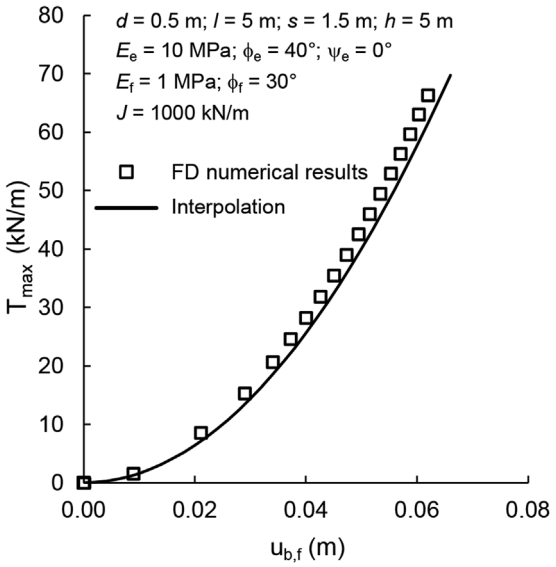

FIGURE 7 Comparison of FD numerical results for the reference case from Mangraviti et al.[35] against the interpolation in terms of T_{max} with $u_{b,f}$.

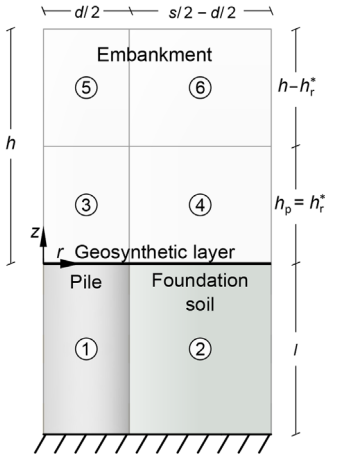

FIGURE 8 Mangraviti et al.[35]: uniform subdomains for GRPS embankments within the unit axisymmetric cell.

subdomains from 3 to 6 evolves during construction. In subdomains 2, 5 and 6 the soil behaves under pseudo-oedometric conditions: stresses and settlements distributions are almost uniform.[35] In subdomains 3 and 4 the arching effect develops (as described in Section 2.2), and, at their interface, strains localise and shear stresses develop (as in Figure 4C).

2.5 | Towards the definition of an upscaled constitutive relationship

According to the numerical results discussed and to the sub-structuring proposed (Figure 8), an upscaled constitutive model, reproducing the mechanical behaviour of the six spatial subdomains, is hereafter defined in agreement with what already done for CPS embankments by di Prisco et al.,[40] where:

A. subdomain 1 is modelled as a rigid element;
B. subdomain 2 as a one-dimensional linear elastic spring;
C. subdomains 3, 4 (see Appendix A), 5 and 6 as one-dimensional geometrically non-linear elastic springs, evolving with h_p;
D. the process zone as a (both mechanically and geometrically) non-linear frictional plastic interface element (see Appendix B).

In case of GRPS embankments, the unique difference with respect to the CPS embankment case is the mechanical response of subdomain 2, composed by both foundation soil and geosynthetic reinforcement.

According to the numerical results: (i) displacements of the membrane and the top of foundation soil are coincident (Figure 6B) and (ii) vertical stresses acting above the membrane (Figure 6A) are partially transmitted to foundation soil ($\sigma_{v,s}$ numerical results in Figure 9A) and geosynthetic reinforcement ($\Delta\sigma_v$ numerical results in Figure 9B). For all these reasons and since the pile is assumed to be rigid, subdomain 2 may be interpreted as an in parallel system (Figure 9C).

In the light of the substructuring approach introduced in Section 2.4, average quantities for displacements ($u_{b,f}$) and stresses (σ_f, $\sigma_{f,s}$ and $\Delta\sigma_f$ in Figures 6A and 9A, B, respectively) are used to reproduce the in parallel system response of subdomain 2 (Figure 9C), where:

$$\Delta\sigma_f = \sigma_f - \sigma_{f,s}. \tag{1}$$

Since axisymmetric conditions are considered, the average values are evaluated as:

$$u_{b,f} = \frac{2\pi \int_{d/2}^{s/2} u\,(r, z=0)\, r dr}{\pi\,(s^2 - d^2)\,/4} \tag{2}$$

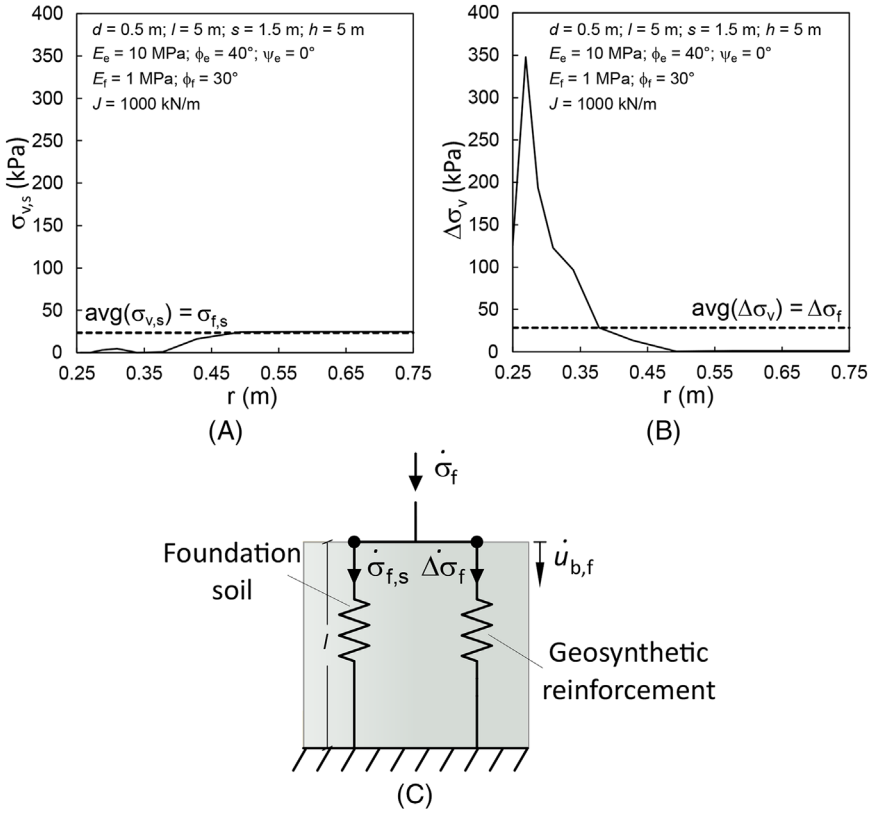

FIGURE 9 Numerical results from Mangraviti et al.[35] in terms of stress profiles acting on: (A) the foundation soil and (B) the geosynthetic reinforcement. (C) In-parallel scheme modelling the mechanical response of subdomain 2 (foundation soil + membrane).

$$\sigma_f = \frac{\int_0^{2\pi}\int_{d/2}^{s/2}\sigma_v(r)\,r\,d\vartheta\,dr}{\pi\left(s^2-d^2\right)/4}, \tag{3}$$

$$\sigma_{f,s} = \frac{\int_0^{2\pi}\int_{d/2}^{s/2}\sigma_{v,s}(r)\,r\,d\vartheta\,dr}{\pi\left(s^2-d^2\right)/4}, \tag{4}$$

$$\Delta\sigma_f = \frac{\int_0^{2\pi}\int_{d/2}^{s/2}\Delta\sigma_v(r)\,r\,d\vartheta\,dr}{\pi\left(s^2-d^2\right)/4}, \tag{5}$$

Due to the increase in stiffness of the membrane working under large displacements, the dependence on $u_{b,f}$ of $\Delta\sigma_f$ is highly non-linear (Figure 10) and is satisfactorily interpolated by a cubic function. This latter will be employed in Section 3.1.1 as one of the ingredients necessary for the definition of the generalised constitutive law.

3 | MATHEMATICAL MODEL FOR GRPS EMBANKMENTS

The model in Figure 11 is conceived by using the following non-dimensional quantities (defined in ref. 40):

$$U_{b,f} = \frac{u_{b,f}}{l}\frac{E_{oed,f}}{\gamma d} \tag{6}$$

$$\Sigma_f = \frac{\sigma_f}{\gamma d} \tag{7}$$

$$U_{t,diff} = U_{t,f} - U_{t,c} = \frac{u_{t,f}-u_{t,c}}{l}\frac{E_{oed,f}}{\gamma d} \tag{8}$$

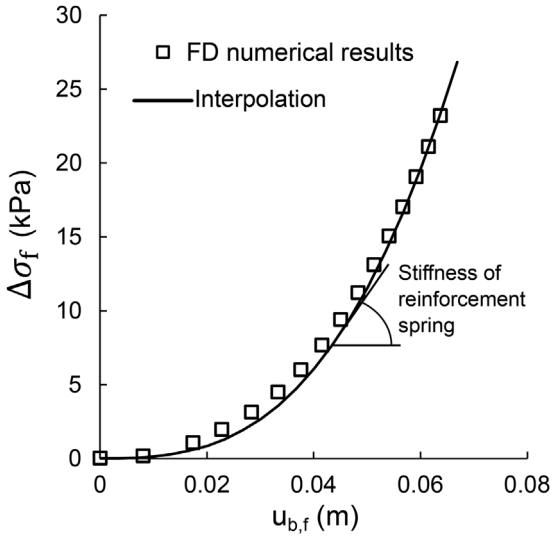

FIGURE 10 Comparison of FD numerical results against cubic interpolation in terms of average stress applied on the membrane and settlements of the membrane.

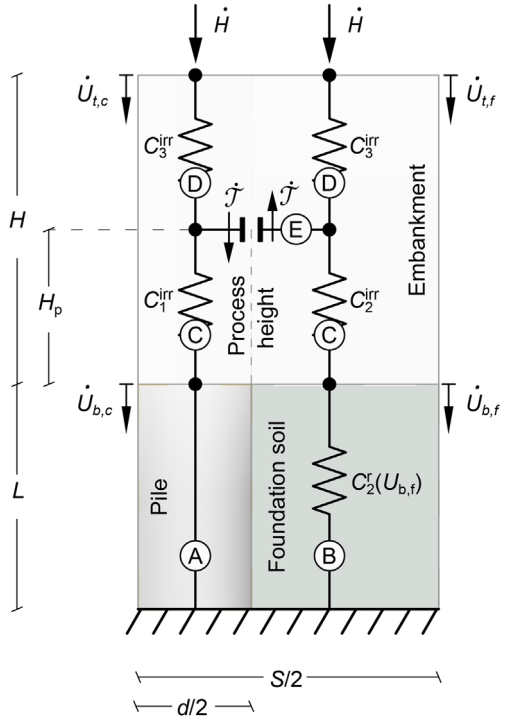

FIGURE 11 Upscaled constitutive model for GRPS embankments.

$$U_{t,av} = \frac{U_{t,f}\left(S^2-1\right)+U_{t,c}}{S^2} = \frac{u_{t,f}\left(s^2-d^2\right)+u_{t,c}d^2}{s^2 l}\frac{E_{oed,f}}{\gamma d} \tag{9}$$

being $E_{\mathrm{oef,f}}$ the foundation soil oedometric modulus, whereas:

$$u_{t,c} = \frac{\int_0^{2\pi}\int_0^{d/2} u\left(r, z=h\right) r\, d\vartheta\, dr}{\pi d^2/4} \quad \text{and} \quad u_{t,f} = \frac{\int_0^{2\pi}\int_{d/2}^{s/2} u\left(r, z=h\right) r\, d\vartheta\, dr}{\pi\left(s^2-d^2\right)/4}. \tag{10}$$

As for the case of CPS embankments,[40] the employment of these non-dimensional variables is particularly convenient since in the non-dimensional $U_{tdiff}H$ (being $H = h/d$ the non-dimensional embankment height) and $U_{tav}H$ planes, the

embankment response is unique if the non-dimensional geometrical ratios ($S = s/d, L = l/d$), the non-dimensional stiffness ratio (E_{oede} E_{oedf}, being E_{oede} the embankment soil oedometric modulus) and the embankment soil failure parameters (ϕ'_e and ψ_e) are kept constant.

For the case of GRPS embankments, an additional non-dimensional variable is introduced:

$$T^*_{max} = \frac{T_{max}}{\gamma d^2} \tag{11}$$

The incremental upscaled constitutive relationship, conceived in the framework of the macroelement approach[80–91] is expressed as it follows:

$$\begin{bmatrix} \dot{U}_{t,diff} \\ \dot{U}_{t,av} \\ \dot{T}^*_{max} \end{bmatrix} = \begin{bmatrix} C_{diff}\left(U_{b,f}\right) \\ C_{av}\left(U_{b,f}\right) \\ J^* D_t\left(U_{b,f}\right) \end{bmatrix} \dot{H}, \tag{12}$$

where dots stand for increments, J^* is the relative reinforcement-foundation soil stiffness:

$$J^* = \frac{Jl}{E_{oed,f} d^2}\ , \tag{13}$$

C_{diff} and C_{av} are two non-dimensional compliances and D_t is a non-dimensional stiffness (defined as in Sections 3.1 and 3.2, respectively). Due to the geometric non-linearity of the membrane response, C_{diff}, C_{av}, and D_t depend on $U_{b,f}$.

3.1 | Definition of C_{diff} and C_{av}

By following the procedure introduced in di Prisco et al.[40] (reported, for the ease of the reader in Appendix C) C_{diff} and C_{av} are:

$$C_{diff}\left(U_{b,f}\right) = C_2^r\left(U_{b,f}\right) + C_2^{irr} - C_1^{irr} - 4\bar{k}\tan\phi'_{ss}\left[C_1^{irr} + \frac{C_2^r\left(U_{b,f}\right) + C_2^{irr}}{(S^2-1)}\right] H_p \tag{14}$$

$$C_{av}\left(U_{b,f}\right) = \frac{C_1^{irr}}{S^2} + \frac{\left[C_2^r\left(U_{b,f}\right) + C_2^{irr}\right](S^2-1)}{S^2} - \frac{4\bar{k}\tan\phi'_{ss} H_p\left[C_2^r\left(U_{b,f}\right) + C_2^{irr} - C_1^{irr}\right]}{S^2} + C_3^{irr} \tag{15}$$

being $H_p = h_p/d$ and ϕ'_{ss} the embankment soil friction angle under simple shear conditions[40,81,87,92–94]:

$$tan\ \phi'_{ss} = \frac{cos\psi_e sin\phi'_e}{1 - sin\psi_e sin\phi'_e}\ . \tag{16}$$

C_1^{irr}, C_2^{irr}, C_3^{irr} are non-dimensional compliances of the proposed constitutive model (Figure 11) that are equal to the ones defined for the case of CPS embankments in di Prisco et al.[40] (see Appendix C).

The definition of the compliance of the reinforced soil, $C_2^r(U_{b,f})$, and the evolution rules for both $U_{b,f}$ and H_p are introduced in Section 3.1.1, 3.1.2 and 3.1.3, respectively.

3.1.1 | Definition of C_2^r

As was previously mentioned, in case of GRPS embankments the mechanical response of subdomain 2 (Figure 8) can be reproduced by employing an in parallel scheme (Figure 9C) whose compliance is a function of $U_{b,f}$ and can be calculated as:

$$C_2^r\left(U_{b,f}\right) = \frac{1}{\frac{1}{C_{2,s}^r} + \frac{1}{C_{2,r}^r\left(U_{b,f}\right)}}\ , \tag{17}$$

being $1/\ C^r_{2,s} = 1$ (due to the non-dimensional variables definitions Equations 6 and 7) the non-dimensional stiffness of the spring representing the foundation soil and $1/C^r_{2,r}$ the non-dimensional stiffness of the spring representing the geosynthetic reinforcement (see Figure 9C). Due to the membrane geometric non-linear behaviour, $1/C^r_{2,r}$ evolves with $U_{b,f}$.

According to the in parallel scheme of Figure 9(C), the expression for $C^r_{2,r}(U_{b,f})$ can be derived from the variation of $\Delta\Sigma_f = \Delta\sigma_f\ /\gamma d$ with $U_{b,f}$:

$$\Delta\dot{\Sigma}_{\mathrm{f}} = \dot{U}_{b,f} \Big/ \left[C^{\mathrm{r}}_{2,r}\left(U_{b,f}\right)\right], \tag{18}$$

being the compliance $C^r_{2,\mathrm{r}}(U_{b,f})$ the inverse of the slope of the curve in Figure 10. As was previously mentioned, the interpolation in Figure 10 is a cubic law, implying that the stiffness (i.e., the slope of the curve) quadratically increases with $U_{b,f}$:

$$\frac{1}{C^r_{2,r}\left(U_{b,f}\right)} = \alpha J^* \left(\frac{\gamma l}{E_{oed,f}}\right)^2 \frac{U^2_{b,f}}{(S-1)^4}, \tag{19}$$

being $\alpha = 250$ a non-dimensional interpolating parameter, calibrated on results of a parametric numerical study (reported in Appendix D).

Equations (17) and (19) put in evidence that, for $J^* = 0$ (i.e., CPS embankments), $C^r_2 = C^r_{2,s}$ and the model introduced by di Prisco et al.[40] is retrieved.

3.1.2 | Definition of the evolution rule for $U_{b,f}$

According to the upscaled model (Figures 11 and 9C):

$$\dot{U}_{b,f} = C^r_2\left(U_{b,f}\right)\dot{\Sigma}_{\mathrm{f}}, \tag{20}$$

where $\dot{\Sigma}_{\mathrm{f}}$ may be calculated by imposing the balance of momentum along the vertical direction:

$$\dot{\boldsymbol{\Sigma}}_{\mathrm{f}} = \dot{H} - \frac{4\dot{\mathcal{T}}}{\pi\left(S^2-1\right)} = \left(1 - \frac{4\bar{k}\tan\phi'_{ss}}{S^2-1}H_p\right)\dot{H}, \tag{21}$$

being $\dot{\mathcal{T}}$ the increment in non-dimensional tangential force transferred by the plastic slider which is element E of Figure 11, (defined as in Equations A1–A3 in Appendix B).

3.1.3 | Definition of the evolution rule for H_p

Analogously to the model for CPS embankments,[40] H_p is interpreted as a generalised hardening variable. Its evolution rule, taking both geometrical and mechanical non-linearities into account, is derived from the numerical results (Figure 2A) as:

$$\dot{H}_p = \begin{cases} \dot{H} & if\ F\left(H, U_{b,f}\right) > 0 \\ 0 & if\ F\left(H, U_{b,f}\right) < 0 \end{cases} \tag{22}$$

The function $F(H, U_{b,f})$ is defined as:

$$F\left(H, U_{b,f}\right) = H^*\left(U_{b,f}\right) - H, \tag{23}$$

being H^* the non–dimensional height of plane of equal settlement. Initially, the ideal position of the plane of equal settlements is above the maximum embankment height ($H^* > H$) and H_p is coincident with H. Subsequently, for a sufficiently large embankment height value, H becomes greater than H^* and H_p stops evolving. Analogously to CPS embankments,[40]

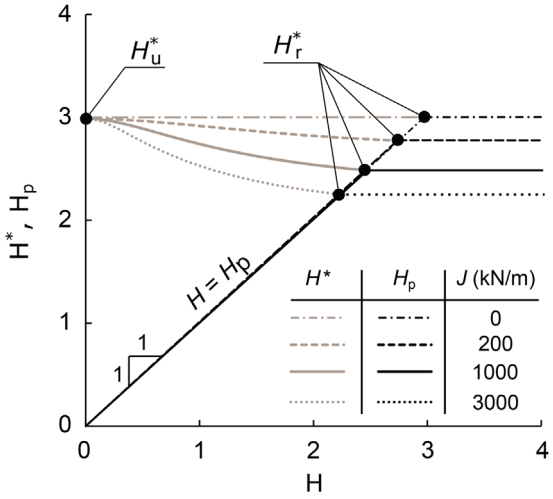

FIGURE 12 Evolution rule of both non-dimensional process height (H_p) and plane of equal settlements (H^*) during construction for the reference case by varying J.

the evolution law of the position of the plane of equal settlements is obtained by imposing $C_{diff} = 0$ (i.e., mathematical definition of plane of equal settlements, see Equation 12) and $H_p = H = H^*$ (as from numerical results, see Figure 2A) into Equation (14):

$$C_{diff} = C_2^r\left(U_{b,f}\right) - 4\bar{k}tan\phi'_{ss}\left[\frac{H^*}{E_{oed,e}}\frac{E_{oed,f}}{L} + \frac{C_2^r\left(U_{b,f}\right) + \frac{H^*}{E_{oed,e}}\frac{E_{oed,f}}{L}}{S^2-1}\right]H^* = 0 \tag{24}$$

that becomes:

$$H^*\left(U_{b,f}\right) = \frac{1}{2}\sqrt{\left[\frac{E_{oed,e}}{E_{oed,f}}\frac{L}{S^2}C_2^r\left(U_{b,f}\right)\right]^2 + \frac{(S^2-1)}{\bar{k}tan\phi'_{ss}}\left(\frac{E_{oed,e}}{E_{oed,f}}\frac{L}{S^2}\right)C_2^r\left(U_{b,f}\right)} - \frac{1}{2}\left(\frac{E_{oed,e}}{E_{oed,f}}\frac{L}{S^2}\right)C_2^r\left(U_{b,f}\right) \tag{25}$$

The initial value of $H^*(U_{b,f} = 0)$ corresponds to the non-dimensional critical height for the unreinforced case, $H^* = H_u^*$ in Figure 12 (obtained when $U_{b,f} = 0$ and $C_2^r = C_{2,s}^r$, Equations 17 and 19). In case of GRPS embankments, due to the progressive embankment construction, $U_{b,f}$ increases and consequently both C_2^r (Equations 17 and 19) and H^* decrease (grey lines Figure 12).

When $H = H_p = H^*$, also H^* stops evolving and the final value of non-dimensional critical height for GRPS embankments ($H^* = H_r^* = h_r^*/d$) is obtained.

It is worth noticing that both the evolution of H^* and the final value H_p depend on the reinforcement stiffness through Equations (17) and (19) (according to what observed in the numerical results, see Figure 2B).

3.2 | Definition of D_t

According to the numerical results reported in Figure 7, not accounting for membrane yielding, the maximum tensile force in the reinforcement quadratically increases with $u_{b,f}$. This implies that the increment of T_{max}^* is a linear function of $U_{b,f}$ and, from the interpolation of the curve in Figure 7, it is:

$$\dot{T}_{max}^* = \beta J^* \frac{\gamma l}{E_{oed,f}}\frac{U_{b,f}}{(S-1)^2}\dot{U}_{b,f}. \tag{26}$$

being $\beta = 24$ a non-dimensional interpolating parameter, calibrated on the results of a numerical parametric study (see Appendix D).

TABLE 3 Geometrical variables.

Pile diameter	Pile spacing	Pile length
d	s	l

TABLE 4 Mechanical properties.

Foundation soil oedometric modulus	Embankment soil oedometric modulus	Embankment soil friction angle	Embankment soil dilatancy angle	Embankment soil unit weight	Reinforcement tensile axial stiffness
$E_{f,oed}$	$E_{e,oed}$	ϕ'_e	ψ_e	γ	J

By substituting Equations (20) and (21) into Equation (26) we obtain:

$$\dot{T}^*_{max} = \beta J^* \frac{\gamma l}{E_{oed,f}} \frac{U_{b,f}}{(S-1)^2} C_2^r \left(U_{b,f}\right) \left(1 - \frac{4\bar{k} \tan \phi'_{ss} H_p}{S^2 - 1}\right) \dot{H}, \tag{27}$$

and therefore:

$$D_t = \beta \frac{\gamma l}{E_{oed,f}} \frac{U_{b,f}}{(S-1)^2} C_2^r \left(U_{b,f}\right) \left(1 - \frac{4\bar{k} \tan \phi'_{ss} H_p}{S^2 - 1}\right). \tag{28}$$

4 | MODEL VERIFICATION

The model proposed by the authors for GRPS embankments is a result of an upscaling procedure, therefore it depends on both (i) geometry (Table 3) and materials mechanical properties (Table 4), that are input data, and (ii) three constitutive parameters ($\bar{k}$, α and β).

As was previously mentioned, $\bar{k}$ is not significantly affected by the presence of the reinforcement.[35] For this reason, $\bar{k}$ can be estimated by using the curve for CPS embankments (Figure 5), where its dependence on the embankment dilatancy angle is reported.

α and β are constant numerically calibrated ($\alpha = 250$ and $\beta = 24$) on the results of the previously mentioned parametric study (see Appendix D).

In Figure 13, the results obtained by integrating the constitutive model (Equation 12) are compared with the numerical results (in terms of evolution of $U_{t,diff}$, $U_{t,av}$, $U_{b,f}$ and T^*_{max} with H) relative to the reference case previously discussed (Tables 1 and 2). The agreement is very satisfactory in terms of displacements, both at the embankment top and base. The model is slightly less accurate in term of maximum tensile force acting in the reinforcement, but it provides a safe side estimation.

In Figure 14, the proposed generalised constitutive model is also verified against the numerical parametric study performed in Mangraviti et al.[35]

The proposed constitutive relationship can very satisfactorily reproduce the numerical results in terms of displacements within a range of error of ±10% (Figure 14A, B). Differential settlement predictions overestimate numerical results only for $S > 4$ up to about 20%.

As far as the maximum tensile force, T_{max}, is concerned (Figure 14C), the predictions are slightly less accurate, but in the cases in which the error is larger than 20% the model provides a safe side estimation.

5 | MODEL VALIDATION

The upscaled constitutive model proposed in the paper is here validated against field measurements. Many researchers have investigated soil arching in GRPS embankments in different field case studies.[14–18,24,25,95] However, only in two of the cited cases,[15,16,25] the test conditions respected the hypothesis at the base of the upscaled constitutive model proposed by the authors. These two cases are discussed in Section 5.1 and 5.2, respectively. Depending on the measurements

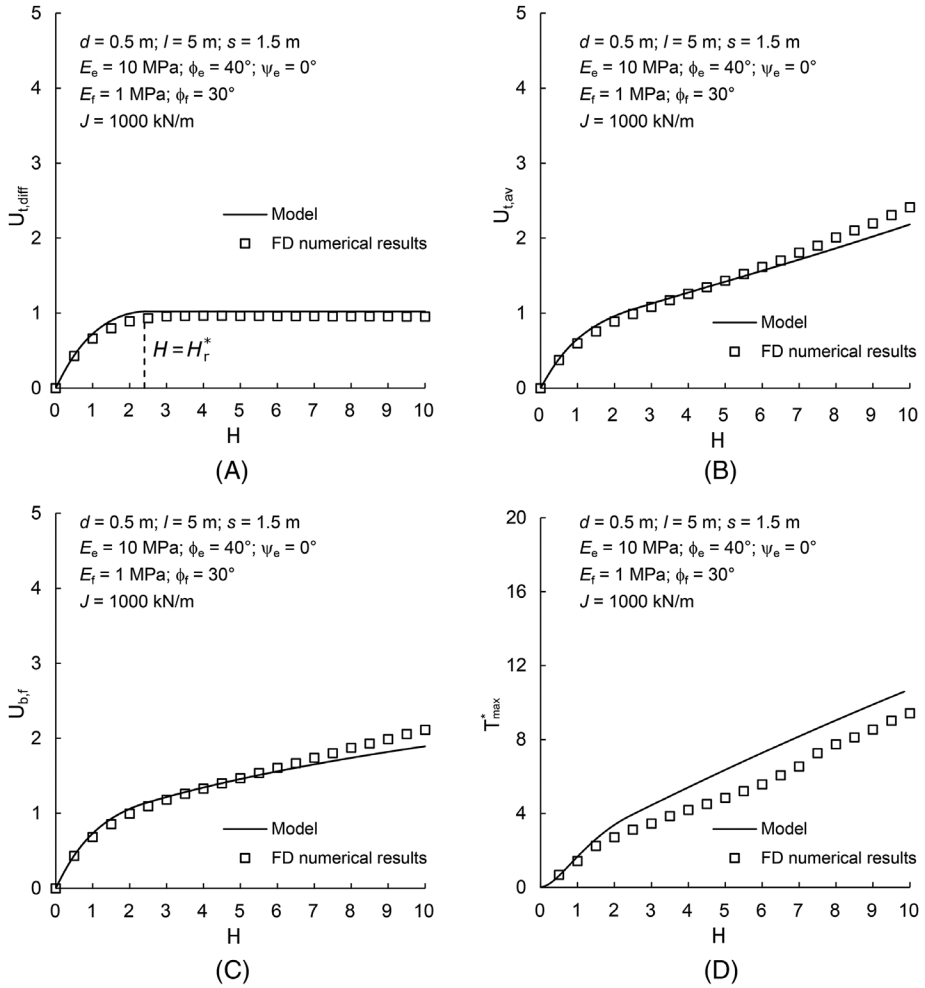

FIGURE 13 Validation of the upscaled constitutive model against FD numerical results in terms of evolution of generalised non-dimensional variables against H: (A) differential and (B) average displacements at the top of the embankment; (C) displacements at the embankment base and (D) tensile force in the membrane.

available, the upscaled constitutive model will be validated in terms of settlements at the base of the embankment (u_{bf}) and maximum tensile force in the geosynthetic ($T_{\max}$).

The validation shows the suitability of the proposed model for being used also for the case of: (i) both triangular and square pile patterns; (ii) layered foundation soils and (iii) piles with pile caps.

5.1 | Large scale experimental test in Incheon

In Oh and Shin,[25] the experimental results of a scale field test campaign, performed at the Geotechnical Experimentation Site of the University of Incheon (Republic of Korea), are illustrated.

The piles are positioned according to a square pattern. Four different tests were performed (Table 5), each one associated with a different pile spacing (s_{ctc}, in Figure 1C). Test 1 refers to an unreinforced embankment with no piles and is used by the authors to calibrate the foundation soil stiffness.

Oh and Shin[25] provide the measurements of the evolution with time of (i) the embankment height and (ii) settlements at the midspan in both horizontal and diagonal direction. The average of the two settlement measurements was used in the following. Unfortunately, settlements at the top and maximum tensile force in the geosynthetic are not measured during the test.

The input data required by the upscaled constitutive model are summarised in Table 6. d is assumed to be coincident with the pile cap diameter from Oh and Shin.[25] The equivalent axisymmetric cell diameter, s, was calculated as in

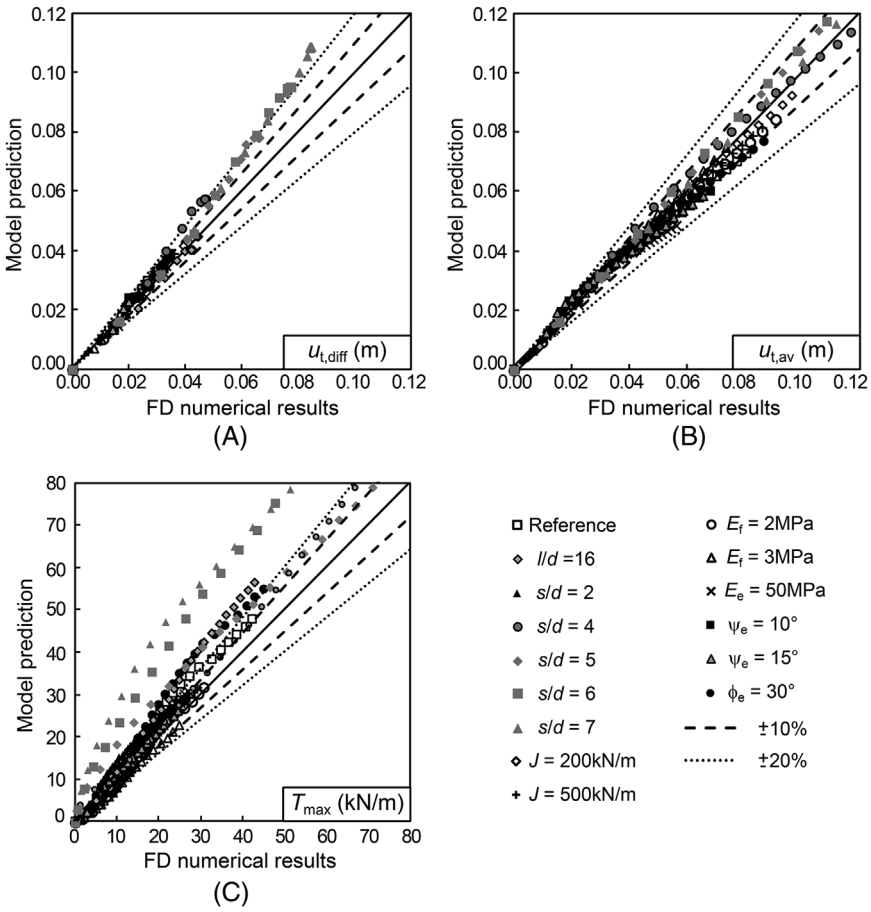

FIGURE 14 Verification of the model against parametric numerical analyses from Mangraviti et al.[35] Comparison in terms of (A) differential and (B) average settlements at the top of the embankment and (C) maximum tensile force in the geosynthetic layer.

TABLE 5 Test conditions considered in Oh and Shin.[25]

Test n.	1	2	3	4
s_{ctc}	–	0.75	0.6	0.95

TABLE 6 Geometry and material properties used in the model for the validation against Oh and Shin[25] field test.

Test	d (m)	s (m)	l (m)	$E_{f,oed}$ (MPa)	E_e (MPa)	ϕ'_e (°)	ψ_e (°)	γ (kN/m^3)	J (kN/m)
2		1.06							
3	0.15	0.85	1.6	0.4	20	35	0	18	800
4		1.34							

McGuire,[61] Figure 1(C). The other geometrical values, geosynthetic stiffness, embankment soil friction angle and unit weight in Table 6 are given in Oh and Shin.[25] To provide a safe side estimation of settlements, $\psi_e = 0$ is employed. This value corresponds to $\bar{k} = 0.83$ (Figure 5). The stiffness of the embankment was also not provided, and the authors assumed a value of 20 MPa, to provide a safe side estimation of settlements. It is worth mentioning that, in this case, E_e value plays a minor role on the predictions since the foundation soil stiffness is very low. To evaluate the foundation soil stiffness, the first measured value of embankment height (h_1) and the corresponding average settlement measured at the base of the embankment in Test 1 ($u_{b,1}^{Test\ 1}$) are used ($E_{oed,f} = l\gamma h_1/u_{b,1}^{Test\ 1}$).

The field measurements are compared in Figure 15 against the dimensional results of the upscaled constitutive model in terms of $u_{b,f}$ (calculated by using Equations 6, 16, 17, 20–22).

In general, a good agreement with field measurements is observed. Test 4 ($S = 9$) is the only case where the model largely overestimates the displacements at the base of the embankment, giving a safe side prediction. As discussed for the verification of the model in terms of differential settlements at the top of the embankment (Figure 14A), the model tends to overestimate settlements for $S > 7$.

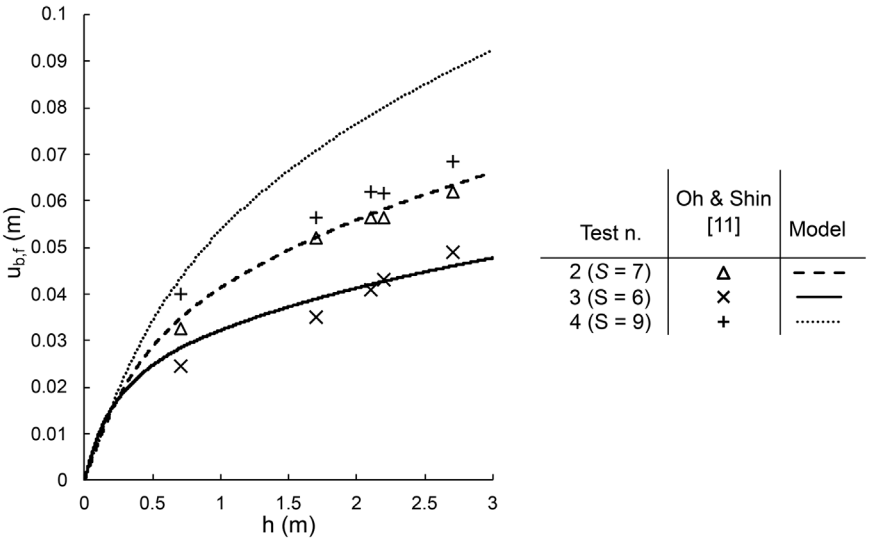

FIGURE 15 Average settlements at the base of GRPS test embankments measured by Oh and Shin[25] compared with model prediction during embankment construction for different values of pile spacing.

TABLE 7 Lu et al.[15,16]: Foundation soil properties of test sections KZ27+350 and KZ27+430.

Sect.	#	Soil layer	Thickness (m)	Depth (m)	Young's Modulus (MPa)
KZ27+350	1	Silty sand silt	0.2	0.2	24.0
	2	Clay	0.6	0.8	6.3
	3	Silt sand	1.3	2.1	12.3
	4	silt	2.8	4.9	7.1
	5	silt sand	11	15.9	33.2
	6	Sand	4	18.9	35.7
KZ27+430	1	Silty sand silt	0.4	0.4	11.3
	2	Clay	0.5	0.9	5.1
	3	Silt sand	0.4	1.3	16
	4	Silt	2.4	3.7	5.8
	5	Silt sand	3.2	6.9	20.4
	6	Sand	4.1	11	38.9
	7	Silt sand	5.9	16.9	34.1
	8	Sand with silt	5.0	21.9	32.6

5.2 | Monitoring of the existing Jiang-Lu highway widening

In Lu et al.,[15,16] the results of field measurements collected during the widening of an existing embankment, previously built on cement deep-mixed piles in Jiang-Lu highway (Yangzhou, China), are illustrated. The existing embankment did not show significant settlements during construction and subsequent consolidation, suggesting that the hydraulic conductivity of the foundation soil was sufficiently large to allow the dissipation of the excess pore water pressure during the construction (drained construction of the embankment). The old embankment was widened by constructing a new GRPS embankment on the sides of the existing one and the measurements relative to two transversal cross-sections (KZ27+350 and KZ27+430) are employed to validate the model in terms of maximum tensile force in the geosynthetic. In particular, the measurements relative to the pile closer to the centre of the embankment (pile S1 in Lu et al.[16]) are considered here below. Unfortunately, data concerning settlements of the new GRPS embankment were not provided by Lu et al.[15,16]

In this case study, the piles are positioned according to a triangular pattern. The two sections are characterised by a stratified foundation soil. The mechanical properties of each layer are reported in Table 7 (from Lu et al.[15,16]).

TABLE 8 Geometry and material properties used in the model for the validation against Lu et al.[16] field tests.

Sect.	*d* (m)	*s* (m)	*l* (m)	$E_{f,oed}$ (MPa)	E_e (MPa)	ϕ'_e (°)	ψ_e (°)	γ (kN/m^3)	*J* (kN/m)
KZ27+350	1.4	2.8	15.9	2.27	15	30	0	20	1100
KZ27+430			16.9	2.31					

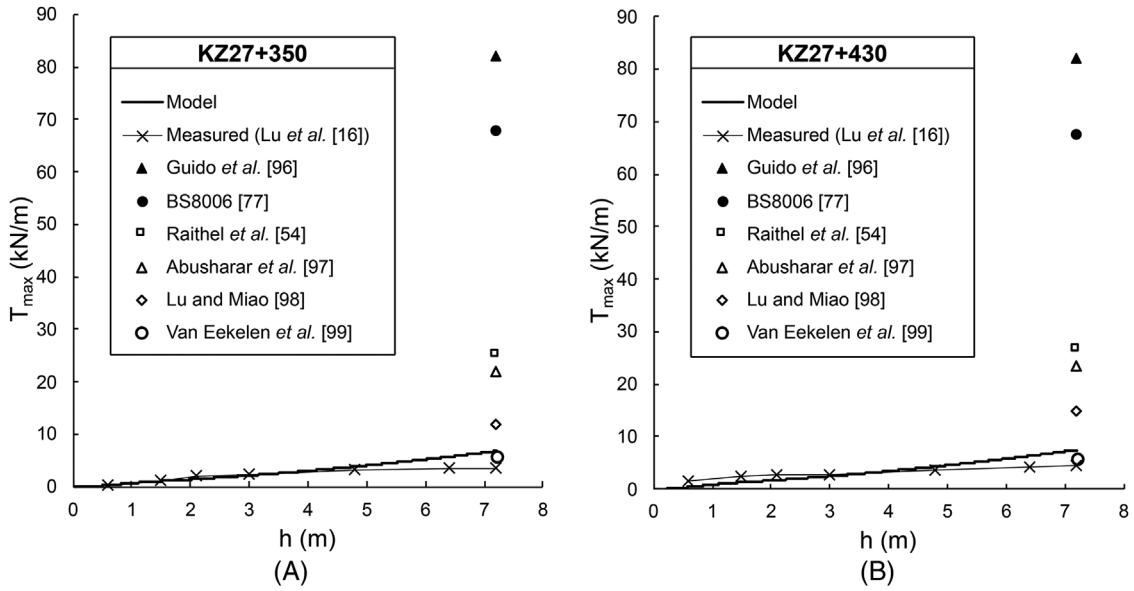

FIGURE 16 Maximum tensile force in the geosynthetic measured by Lu et al.[16] during construction compared with model predictions for both sections (A) KZ27+350 and (B) KZ27+430.

Since the upscaled model is conceived for homogeneous foundation soils, the authors have first calculated the average value of stiffness as it follows :

$$\frac{l}{E_{oed,f}} = \sum_{i=1}^{n} \frac{l_i}{E_{oed,f}^{layeri}} \tag{29}$$

being $E_{oed,f}^{layer\ i}$ and l_i the oedometric stiffness modulus and the thickness of the *i*-th soil layer (Table 7). *n* is the total number of layers.

All the input data required by the upscaled constitutive model are summarised in Table 8. Geometrical values, geosynthetic stiffness, embankment soil mechanical properties are given by Lu et al.[16] In particular, *d* is assumed to be coincident with the pile cap diameter, whereas the equivalent axisymmetric cell diameter, *s*, was calculated as in McGuire,[61] Figure 1(B). Also in this case, to be on the safe side, ψ is imposed equal to zero ($\bar{k} = 0.83$, Figure 5).

The model blind predictions (all the model input data in Table 8 are directly taken from Lu et al.[16]) are compared in Figure 16 against field measurements for both cross-sections in terms of T_{max} (Equations 11 and 12) during construction. The agreement is satisfactory, even if predictions slightly overestimate the in situ data.

For the sake of completeness, in Figure 16, also the predictions of T_{max}, reported by Lu et al.,[16] estimated by employing some existing methods available in literature (Guido et al.,[96] BS8006,[77] Raithel et al.,[54] Abusharar,[97] Lu and Miao[98] and van Eekelen et al.[45]) are plotted. All the approaches, except the one proposed by van Eekelen et al.,[45] enormously overestimate T_{max}, potentially leading to an overconservative design of the intervention.

TABLE 9 Mechanical properties for the practical example.

$E_{f,oed}$ (MPa)	$E_{e,oed}$ (MPa)	ϕ'_e (°)	ψ_e (°)	γ (kN/m^3)
2.7	20	35	10	18

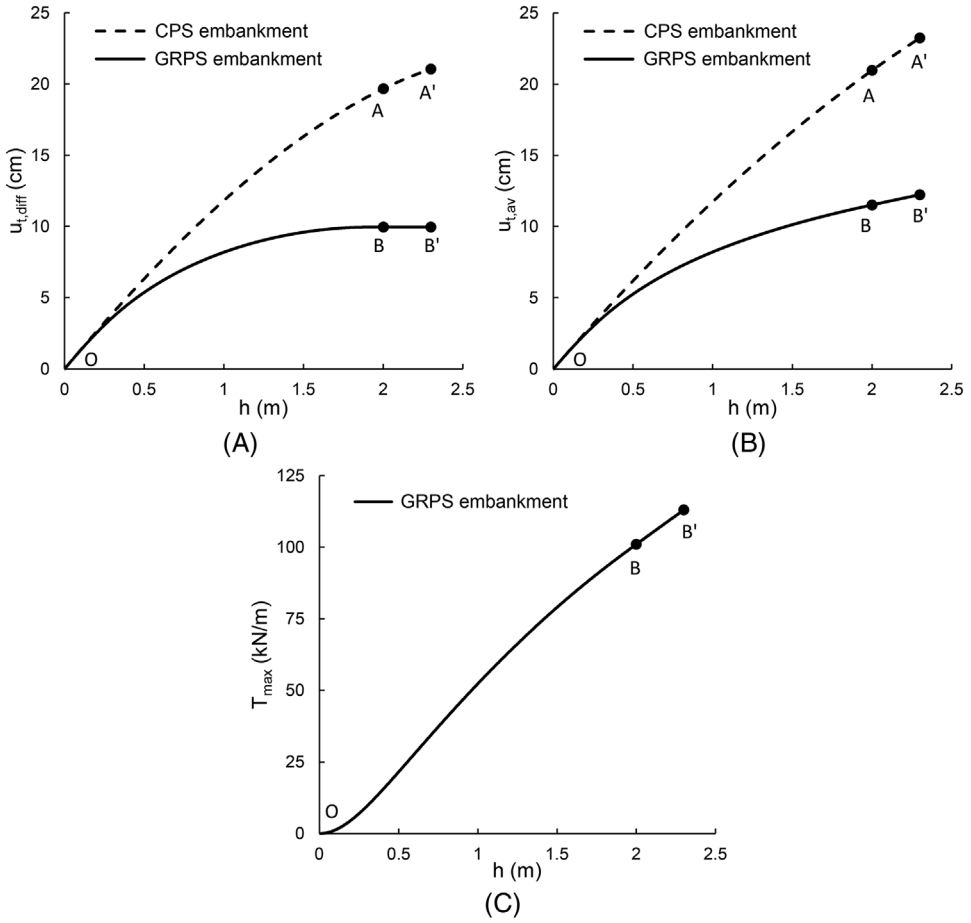

FIGURE 17 Practical example: model previsions in terms of (A) differential settlements at the embankment top, (B) average settlements at the embankment top and (C) tensile force acting in the reinforcement.

6 | PRACTICAL APPLICATION

To exemplify the practical employment of the proposed model, it is used as a preliminary design tool in relation to the construction of a pile supported 2 m thick embankment, on the top of which 30 cm of railway ballast is positioned. In the proposed model the ballast is interpreted as an increment in the final embankment height (i.e., to provide a safe side estimation, the ballast and the embankment are assumed to be characterised by the same unit weight and stiffness values). The embankment is assumed to be positioned above a 20 m thick soft soil stratum.

The foundation soil and the embankment mechanical properties are enlisted in Table 9.

Pile diameter and spacing are assumed to be assigned ($d = 0.5$ m and $s = 3$ m) and, for the sake of brevity, only two different design solutions are discussed. In the first one the base of the embankment is not reinforced, whereas in the second case a geosynthetic reinforcement ($J = 3868$ kN/m, as in van Eekelen et al.[38]) is used.

The results obtained by means of the proposed model are reported in Figure 17. In particular, the results in terms of dimensional $u_{t,diff}$, $u_{t,av}$ and T_{max} are in Figure 17(A–C), respectively.

The whole construction process is subdivided into two phases: the first one (OA and OB for the unreinforced and the reinforced cases, respectively) is associated with the embankment construction, whereas the second one (AA' and BB' for the unreinforced and the reinforced cases, respectively) to the ballast deposition.

The results clearly highlight that in GRPS embankment case the differential displacement increment due to the ballast construction (BB') is nil. In contrast, in the unreinforced case (AA') it is equal to 1.4 cm, suggesting that, in this case, the CPS embankment is not suitable for practical purposes.

As far as average displacements are concerned (Figure 17B), the increment in the GRPS case is equal to 0.7 cm, whereas in the CPS case to 2.3 cm.

Moreover, the results in Figure 17(C) highlight that the final value of the tensile force is equal to 113 kN/m, approximately equal to the 30% of the ultimate tensile strength of the reinforcement.[38] Under this tensile force value, the adopted reinforcement is still characterised by a linear response.[38]

7 | CONCLUDING REMARKS

In this paper, the authors propose a new generalised constitutive relationship, following the axisymmetric unit cell approach, based on both the concept of plane of equal settlements and a sub-structuring of the spatial domain. The model here proposed considers end-bearing piles and a smooth interface between piles and homogeneous foundation soil (layered foundation soil can be modelled by using an equivalent stiffness value). The model has been shown to be capable of reproducing the mechanical response of GRPS embankments during the embankment construction, obtained by performing large-displacement finite difference numerical analyses. The model, simulating a layer-by-layer drained embankment construction, can assess, once geometry and mechanical properties are assigned, (i) both average and differential settlements induced by the embankment construction and (ii) the maximum tensile force within the reinforcement. Furthermore, it has been validated against two field measurements series taken from the literature. The comparison of the model results with field test data showed that the model predictions are accurate for spacing over pile diameter ratio lower than seven. For larger spacing over pile diameter ratios, the model gives safe side predictions by overestimating both settlements and tensile forces in the geosynthetic. The model proposed by the authors, allowing to estimate the system performance with a negligible time (few seconds) and computational efforts, may be employed as a tool in the pre-design stage for optimising geometry (pile diameter and spacing) and choose reinforcement mechanical properties. The model can be extended to the case of floating piles and rough pile-soil interface by defining and calibrating new additional elements.

LIST OF NOTATIONS

C_{av}, C_{diff}	non-dimensional compliances of the constitutive model
C_1^{irr}, C_2^{irr}, C_3^{irr}	non-dimensional compliances from di Prisco et al.[40]
$C_{2,r}^{r}$, $C_{2,s}^{r}$	non-dimensional compliance of the springs representing the reinforcement and of the foundation soil, respectively (Equation 17)
C_2^r	non-dimensional compliance of the reinforced soil (subdomain 2, see Figure 11)
d	pile diameter
D_t	non-dimensional function of the constitutive model
E_e	embankment soil Young's modulus
E_f	foundation soil Young's modulus
$E_{oed,e}$	embankment soil oedometric modulus
$E_{oed,f}$	foundation soil oedometric modulus
$E_{oed,f}^{layer\ i}$	oedometric stiffness modulus of the i-th foundation soil layer (Table 7)
F	function of H and H^* (Equation 23)
H	non-dimensional embankment height
h	embankment height
H^*	non-dimensional evolution law of the height of the plane of equal settlements
h_1	first measured value of embankment height in Oh and Shin[11]
H_p	non-dimensional height of the shear zone
h_p	height of the shear zone
H_r^*	non-dimensional critical embankment height for reinforced case
h_r^*	dimensional critical embankment height for reinforced case
H_u^*	non-dimensional critical embankment height for unreinforced case

J	geosynthetic tensile axial stiffness
J^*	non-dimensional geosynthetic tensile axial stiffness
k	ratio between horizontal and vertical stresses
$\bar{k}$	average value of k in the process zone
L	non-dimensional pile length
l	pile length and soft soil stratum thickness
l_i	thickness of the i-th foundation soil layer (Table 7)
$\mathcal{N}$	normal force acting on the shear zone
n	the total number of foundation soil layers
r	radial coordinate (Figure 1B)
S	non-dimensional pile spacing
s	unit cell diameter
s_{ctc}	centre-to-centre pile spacing
T	tensile force (per unit length) within the geosynthetic
$T_{\max}$	maximum value of T
T^*_{max}	non-dimensional maximum tensile force within the geosynthetic
u	vertical displacement
$U_{b,f}$	non-dimensional average settlement of the base of subdomain 4 (Figure 8)
$u_{b,f}$	average settlement of the base of subdomain 4 (Figure 8)
u_m	membrane settlement
$U_{t,av}$	non-dimensional average settlement at the top of the embankment
$u_{t,av}$	non-dimensional average settlement at the top of the embankment
$U_{t,c}$	non-dimensional average settlement of the top of subdomain 5 (Figure 8)
$u_{t,c}$	average displacement of the top of subdomain 5 (Figure 8)
$U_{t,diff}$	non-dimensional differential settlement at the top of the embankment
$u_{t,diff}$	dimensional differential settlement at the top of the embankment
$U_{t,f}$	non-dimensional average displacement of the top of subdomain 6 (Figure 8)
$u_{t,f}$	average displacement of the top of subdomain 6 (Figure 8)
$u_{b,1}^{Test\ 1}$	initial average settlement measured at the base of the embankment in Test 1 (Table 5)
z	vertical coordinate (Figure 1A)
α and β	interpolating parameters in Equations (19) and (26)
γ	embankment soil unit weight
$\Delta\Sigma_f$	non-dimensional net average vertical stress transmitted to the geosynthetic reinforcement at the top of subdomain 2 (Figure 8)
$\Delta\sigma_f$	average net vertical stress transmitted to the geosynthetic reinforcement at the top of subdomain 2 (Figure 8)
$\Delta\sigma_v$	net vertical stress transmitted to the geosynthetic reinforcement
Σ_c	non-dimensional average vertical stress on the top of the pile, subdomain 1 (Figure 8)
σ_c	average vertical stress acting above the concrete pile
Σ_f	non-dimensional average vertical stress at the base of subdomain 4 (Figure 8)
σ_f	average vertical stress acting above the membrane
$\sigma_{f,s}$	average vertical stress transmitted by the membrane to the foundation soil
σ_h	horizontal stress
σ_v	vertical stress
$\sigma_{v,s}$	vertical stress transmitted by the membrane to the foundation soil
ϕ'_e	embankment soil internal friction angle
ϕ'_f	foundation soil internal friction angle
ϕ'_{ss}	embankment soil simple shear friction angle
$\mathcal{T}$	non-dimensional tangential force transferred by the plastic slider
τ	tangential stress
ψ_e	embankment soil dilatancy angle
ϑ	angular coordinate of the axisymmetric cell

ACKNOWLEDGEMENTS

Viviana Mangraviti gratefully acknowledges the support of the NordForsk project #98335 NordicLink.

DATA AVAILABILITY STATEMENT

The data that support the findings of this study are available from the corresponding author upon reasonable request.

ORCID

Viviana Mangraviti https://orcid.org/0000-0003-3385-1883
Luca Flessati https://orcid.org/0000-0002-9586-3057
Claudio di Prisco https://orcid.org/0000-0002-9245-6587

REFERENCES

1. Reshma B, Rajagopal K, Viswanadham BVS. Centrifuge model studies on the settlement response of geosynthetic piled embankments. *Geosynth Int*. 2020;27(2):170-181. doi:10.1680/jgein.19.00009
2. Girout R, Blanc M, Thorel L, Dias D. Geosynthetic reinforcement of pile-supported embankments. *Geosynth Int*. 2018;25(1):37-49. doi:10.1680/jgein.17.00032
3. Fagundes DF, Almeida MSS, Thorel L, Blanc M. Load transfer mechanism and deformation of reinforced piled embankments. *Geotext Geomembranes*. 2017;45(2):1-10. doi:10.1016/j.geotexmem.2016.11.002
4. Girout R, Blanc M, Thorel L, Fagundes DF, Almeida MSS. Arching and deformation in a piled embankment: centrifuge tests compared to analytical calculations. *J Geotech Geoenvironmental Eng*. 2016;142(12):04016069. doi:10.1061/(ASCE)GT.1943-5606.0001557
5. Iglesia GR. *Trapdoor Experiments on the Centrifuge–a Study of Arching in Geomaterials and Similitude in Geotechnical Models*. Massachusetts Institute of Technology; 1991.
6. Dewoolkar MM, Santichaianant K, Ko H-Y. Centrifuge modeling of granular soil response over active circular trapdoors. *Soils Found*. 2007;47(5):931-945. doi:10.3208/sandf.47.931
7. Terzaghi. Stress distribution in dry and in saturated sand above a yielding trap-door. In: *International Society for Soil Mechanics and Geotechnical Engineering*; 1936:536-537.
8. Ladanyi B, Hoyaux B. A study of the trap-door problem in a granular mass: discussion. *Can Geotech J*. 1969;6(4):441-443. doi:10.1139/t69-044
9. Vardoulakis I, Graf B, Gudehus G. Trap-door problem with dry sand: a statical approach based upon model test kinematics. *Int J Numer Anal Methods Geomech*. 1981;5(1):57-78. doi:10.1002/nag.1610050106
10. Rui R, Han J, van Eekelen SJM, Wan Y. Experimental investigation of soil-arching development in unreinforced and geosynthetic-reinforced pile-supported embankments. *J Geotech Geoenvironmental Eng*. 2019;145(1):04018103. doi:10.1061/(asce)gt.1943-5606.0002000
11. Hoppe EJ, Hite SL, Performance of a Pile-Supported Embankment; 2006.
12. Almeida MSS, Ehrlich M, Spotti AP, Marques MES. Embankment supported on piles with biaxial geogrids. *Proc Inst Civ Eng - Geotech Eng*. 2007;160(4):185-192. doi:10.1680/geng.2007.160.4.185
13. Van Eekelen SJM, Bezuijen A, Alexiew D, The Kyoto Road piled embankment: 31/2 years of measurements. in *9th International Conference on Geosynthetics - Geosynthetics: Advanced Solutions for a Challenging* World, ICG 2010; 2010:1941-1944.
14. Briançon L, Simon B. Performance of pile-supported embankment over soft soil: full-scale experiment. *J Geotech Geoenviron Eng*. 2012;138(4):551-561. doi:10.1061/(ASCE)GT.1943-5606.0000561
15. Lu WH, Miao LC, Wang F, Cai HS, Zhang CX. Experimental study of soil arching of geogrid-reinforced and pile-supported widening embankment. *Yantu Lixue/Rock Soil Mech*. 2013;34(8).
16. Lu W, Miao L, Wang F, Zhang J, Zhang Y, Wang H. A case study on geogrid-reinforced and pile-supported widened highway embankment. *Geosynth Int*. 2020;27(3):261-274. doi:10.1680/jgein.19.00024
17. Feng S, Xu R, Yu J, Zhang C, Cheng K. Field monitoring of geogrid-reinforced and pile-supported embankment at bridge approach. *Int J Geosynth Gr Eng*. 2021;7(1). doi:10.1007/s40891-020-00248-5
18. Van Duijnen PG, Van Eekelen SJM, Van Der Stoel AEC, Monitoring of a railway piled embankment. In: *9th International Conference on Geosynthetics - Geosynthetics: Advanced Solutions for a Challenging* World, ICG 2010; 2010:1461-1464.
19. Vinet L, Zhedanov A. A 'missing' family of classical orthogonal polynomials. *Diss Dr Philos*. 2010;44:085201. doi:10.1088/1751-8113/44/8/085201
20. Nunez MA, Briançon L, Dias D. Analyses of a pile-supported embankment over soft clay: full-scale experiment, analytical and numerical approaches. *Eng Geol*. 2013;153:53-67. doi:10.1016/j.enggeo.2012.11.006
21. Liu HL, Ng CWW, Fei K. Performance of a geogrid-reinforced and pile-supported highway embankment over soft clay: case study. *J Geotech Geoenviron Eng*. 2007;133(12):1483-1493. doi:10.1061/(asce)1090-0241(2007)133:12(1483)
22. Lai H-J, Zheng J-J, Zhang R-J, Cui M-J. Classification and characteristics of soil arching structures in pile-supported embankments. *Comput Geotech*. 2018;98:153-171. doi:10.1016/j.compgeo.2018.02.007
23. Zhang C, Jiang G, Liu X, Buzzi O. Arching in geogrid-reinforced pile-supported embankments over silty clay of medium compressibility: field data and analytical solution. *Comput Geotech*. 2016;77:11-25. doi:10.1016/j.compgeo.2016.03.007
24. van Eekelen SJM, Venmans AAM, Bezuijen A, van Tol AF. Long term measurements in the Woerden geosynthetic-reinforced pile-supported embankment. *Geosynth Int*. 2020;27(2):142-156. doi:10.1680/jgein.17.00022

25. Oh YI, Shin EC. Reinforcement and arching effect of geogrid-reinforced and pile-supported embankment on marine soft ground. *Mar Georesources Geotechnol*. 2007;25(2):97-118. doi:10.1080/10641190701359591
26. Han J, Gabr MA. Numerical analysis of geosynthetic-reinforced and pile-supported earth platforms over soft soil. *J Geotech Geoenviron Eng*. 2002;128(1):44-53. doi:10.1061/(ASCE)1090-0241(2002)128:1(44)
27. Stewart ME, Filz GM. Influence of clay compressibility on geosynthetic loads in bridging layers for column-supported embankments. *Contemporary Issues in Foundation Engineering*; 2005:1-14. doi:10.1061/40777(156)8
28. Yan L, Yang JS, Han J. Parametric study on geosynthetic-reinforced pile-supported embankments. *Adv Earth Struct*. 2006:255-261. doi:10.1061/40863(195)28
29. Abdullah CH, Edil TB. Numerical analysis of catenary load transfer platform for Geopier-supported embankment. *Advances in Measurement and Modeling of Soil Behavior*; 2007:1-10. doi:10.1061/40917(236)11
30. Potts V, Zdravkovic L. Finite-element study of arching behaviour in reinforced fills. *Proc Inst Civ Eng Gr Improv*. 2010;163(4):217-229. doi:10.1680/grim.2010.163.4.217
31. Ariyarathne P, Liyanapathirana DS, Leo CJ. Comparison of different two-dimensional idealizations for a geosynthetic-reinforced pile-supported embankment. *Int J Geomech*. 2013;13(6):754-768. doi:10.1061/(asce)gm.1943-5622.0000266
32. Yapage NNS, Liyanapathirana DS. A parametric study of geosynthetic-reinforced column-supported embankments. *Geosynth Int*. 2014;21(3):213-232. doi:10.1680/gein.14.00010
33. Rowe RK, Liu KW. Three-dimensional finite element modelling of a full-scale geosynthetic-reinforced, pile-supported embankment. *Can Geotech J*. 2015;52(12):2041-2054. doi:10.1139/cgj-2014-0506
34. Wijerathna M, Liyanapathirana DS. Load transfer mechanism in geosynthetic reinforced column-supported embankments. *Geosynth Int*. 2020;27(3):236-248. doi:10.1680/jgein.19.00022
35. Mangraviti V, Flessati L, di Prisco C. Geosynthetic-reinforced and pile-supported embankments: theoretical discussion of finite elements numerical analyses results. *Eur J Environ Civ Eng*. 2023:1-27. doi:10.1080/19648189.2023.2190400
36. Chen RP, Chen YM, Han J, Xu ZZ. A theoretical solution for pile-supported embankments on soft soils under one-dimensional compression. *Can Geotech J*. 2008;45(5):611-623. doi:10.1139/T08-003
37. Plaut RH, Filz GM. Analysis of geosynthetic reinforcement in pile-supported embankments. Part III: axisymmetric model. *Geosynth Int*. 2010;17(2):77-85. doi:10.1680/gein.2010.17.2.77
38. van Eekelen SJM, Bezuijen A, van Tol AF. Analysis and modification of the British Standard BS8006 for the design of piled embankments. *Geotext Geomembranes*. 2011;29(3):345-359. doi:10.1016/j.geotexmem.2011.02.001
39. Bhasi A, Rajagopal K. Geosynthetic-reinforced piled embankments: comparison of numerical and analytical methods. *Int J Geomech*. 2015;15(5):04014074. doi:10.1061/(asce)gm.1943-5622.0000414
40. di Prisco C, Flessati L, Frigerio G, Galli A. Mathematical modelling of the mechanical response of earth embankments on piled foundations. *Géotechnique*. 2020;70(9):755-773. doi:10.1680/jgeot.18.P.127
41. di Prisco C, Flessati L, Galli A, Mangraviti V, A Simplified Approach for the Estimation of Settlements of Earth Embankments on Piled Foundations. 40; 2020.
42. Mangraviti V, Theoretical modelling of embankments based on piled foundations, PhD thesis, Politecnico di Milano; 2021.
43. Flessati L, di Prisco C, Corigliano M, Mangraviti V. A simplified approach to estimate settlements of earth embankments on piled foundations: the role of pile shaft roughness. *Eur J Environ Civ Eng*. 2023;27(1):194-214. doi:10.1080/19648189.2022.2035259
44. Mangraviti V, Flessati L, di Prisco C. A rheological model for georeinforced embankments based on piled foundations. *IOP Conf Ser Mater Sci Eng*. 2022;1260(1):012014. doi:10.1088/1757-899X/1260/1/012014
45. van Eekelen SJM, Bezuijen A, van Tol AF. An analytical model for arching in piled embankments. *Geotext Geomembranes*. 2013;39:78-102. doi:10.1016/j.geotexmem.2013.07.005
46. Carlsson B, Reinforced Soil, Principles for Calculation. *Terratema AB, Linköping*. Linköping (in Swedish); 1987.
47. Rogbeck Y, Gustavsson S, Sodergren I, Lindquist D, Reinforced piled embankments in Sweden – Design aspects. In: *Proceedings, Sixth International Conference on Geosynthetics*; 1998: 755-762.
48. Svanø G, Ilstad T, Eiksund G, Want A, Alternative calculation principle for design of piled embankments with base reinforcement. In: *Proceedings of the 4th Ground Improvement Geosystems in Helsinki*; 2000.
49. Collin JG, Jie H, Jie H, Design recommendations for column-supported embankments; 2006.
50. Van Eekelen SJM, Bezuijen A, Oung O, Arching in piled embankments; experiments and design calculations. *BGA Int. Conf. Found. Innov. Obs. Des. Pract.*; 2003: 885-894.
51. Hewlett W, Randolph M. Analysis of piled embankments. *Gr Eng*. 1988;21(3):3-7.
52. Low BK, Tang SK, Choa V. Arching in piled embankments. *J Geotech Eng*. 1994;120(11):1917-1938. doi:10.1061/(ASCE)0733-9410(1994)120:11(1917)
53. Zaeske D. *Zur Wirkungsweise von unbewehrten und bewehrten mineralischen Tragschichten über pfahlartigen Gründungselementen*. Univ. Gh Kassel; 2001.
54. Raithel M, Kirchner A, Kempfert HG, German recommendations for reinforced embankments on pile-similar elements. in Geosynthetics in Civil and Environmental Engineering - Geosynthetics Asia 2008: Proceedings *of the 4th Asian Regional Conference on Geosynthetics*; 2008: 697-702. doi:10.1007/978-3-540-69313-0_128
55. Marston A, The Theory of Loads on Pipe in Ditches and Tests of Cement and Clay Drain Tile and Sewer Pipe; 1913.
56. Terzaghi K. *Theoretical Soil Mechanics*. John Wiley & Sons, Inc.; 1943.

57. McKelvey JA. The anatomy of soil arching. *Geotext Geomembranes*. 1994;13(5):317-329. doi:10.1016/0266-1144(94)90026-4
58. Russell D, Pierpoint N. An assessment of design methods for piled embankments. *Gr Eng*. 1997;30(10):39-44.
59. Naughton PJ, The Significance of Critical Height in the Design of Piled Embankments; 2007: 1-10. doi:10.1061/40916(235)3
60. Yun-min C, Wei-ping C, Ren-peng C. An experimental investigation of soil arching within basal reinforced and unreinforced piled embankments. *Geotext Geomembranes*. 2008;26(2):164-174. doi:10.1016/j.geotexmem.2007.05.004
61. McGuire MP. *Critical height and surface deformation of column-supported embankments*. Virginia Polytechnic Institute and State University; 2011.
62. King DJ, Bouazza A, Gniel JR, Rowe RK, Bui HH. Serviceability design for geosynthetic reinforced column supported embankments. *Geotext Geomembranes*. 2017;45(4):261-279. doi:10.1016/j.geotexmem.2017.02.006
63. Filz GM, Smith ME. *Final Contract Report Design of Bridging Layers in Geosynthetic-Reinforced*. Column-Supported Embankments; 2006. https://vtechworks.lib.vt.edu/handle/10919/46681
64. Filz G, Sloan J, McGuire MP, Collin J, Smith M. Column-supported embankments: settlement and load transfer. *Geotechnical Engineering State of the Art and Practice*. 2012:54-77. doi:10.1061/9780784412138.0003
65. Filz GM, Sloan JA, McGuire MP, Smith M, Collin J. Settlement and vertical load transfer in column-supported embankments. *J Geotech Geoenviron Eng*. 2019;145(10). doi:10.1061/(ASCE)GT.1943-5606.0002130
66. Flessati L. Application of an innovative displacement based design approach for earth embankments on piled foundations. In: Barla M, Di Donna A, Sterpi D, eds. *Lecture Notes in Civil Engineering*. Springer International Publishing; 2021:293-299.
67. Itasca, FLAC3D v.6.0—Fast Lagrangian Analysis of Continua in Three Dimensions_, User Manual. *Itasca Consulting Group, Minneapolis*; 2017.
68. Mangraviti V. Displacement-based design of geosynthetic-reinforced pile-supported embankments to increase sustainability. SpringerBriefs in Applied Sciences and Technology, 2022;83-96. doi:10.1007/978-3-030-99593–5_7
69. di Prisco C, Flessati L, Galli A, Mangraviti V. A simplified approach for the estimation of settlements of earth embankments on piled foundations. In: Calvetti F, Cotecchia F, Galli A, Jommi C, eds. *Lecture Notes in Civil Engineering*. Springer International Publishing; 2020:640-648.
70. Mangraviti V, Flessati L, di Prisco C. Modelling the development of settlements of earth embankments on piled foundations. *Lecture Notes in Civil Engineering*. 2021:811-816.
71. Ambily AP, Gandhi SR. Behavior of stone columns based on experimental and FEM analysis. *J Geotech Geoenvironmental Eng*. 2007;133(4):405-415. doi:10.1061/(asce)1090-0241(2007)133:4(405)
72. Huang J, Han J. Two-dimensional parametric study of geosynthetic-reinforced column-supported embankments by coupled hydraulic and mechanical modeling. *Comput Geotech*. 2010;37(5):638-648. doi:10.1016/j.compgeo.2010.04.002
73. Han J, Oztoprak S, Parsons RL, Huang J. Numerical analysis of foundation columns to support widening of embankments. *Comput Geotech*. 2007;34(6):435-448. doi:10.1016/j.compgeo.2007.01.006
74. Zhuang Y, Cheng X, Wang K. Analytical solution for geogrid-reinforced piled embankments under traffic loads. *Geosynth Int*. 2020;27(3):249-260. doi:10.1680/jgein.19.00023
75. Boschi K, di Prisco C, Flessati L, Galli A, Tomasin M. Punching tests on deformable facing structures: numerical analyses and mechanical interpretation. *Lecture Notes in Civil Engineering*. Springer International Publishing; 2020:429-437.
76. Da Silva Burke TS, Elshafie MZEB. Arching in granular soils: experimental observations of deformation mechanisms. *Geotechnique*. 2021;71(10):866-878. doi:10.1680/jgeot.19.P.174
77. BS8006-1. *Code of practice for strengthened/reinforced soils and other fills*. British Standards Institution; 2010:160-209.
78. EBGEO. *Empfehlungen für den Entwurf und die Berechnung von Erdkörpern mit Bewehrungen aus Geokunststoffen - EBGEO*. Wiley-VCH Verlag GmbH & Co. KGaA; 2010.
79. CUR226. *Design Guideline Basal Reinforced Piled Embankments*. CRC Press; 2016.
80. Montrasio L, Nova R. Settlements of shallow foundations on sand: geometrical effects. *Geotechnique*. 1997;47(1):49-60. doi:10.1680/geot.1997.47.1.49
81. di Prisco C, Flessati L. Progressive failure in elastic–viscoplastic media: from theory to practice. *Géotechnique*. 2021;71(2):153-169. doi:10.1680/jgeot.19.P.045
82. Nova R, Montrasio L. Settlements of shallow foundations on sand. *Géotechnique*. 1991;41(2):243-256.
83. di Prisco C, Flessati L. A generalized constitutive relationship for undrained soil structure interaction problems. *Lecture Notes in Civil Engineering*. 2021. doi:10.1007/978-3-030-64514-4_37
84. Gottardi G, Houlsby GT, Butterfield R. Plastic response of circular footings on sand under general planar loading. *Geotechnique*. 1999;49(4):453-469. doi:10.1680/geot.1999.49.4.453
85. Cremer C, Pecker A, Davenne L. Modelling of nonlinear dynamic behaviour of a shallow strip foundation with macro-element. *J Earthq Eng*. 2002;6(2):175-211. doi:10.1080/13632460209350414
86. Grange S, Kotronis P, Mazars J. A macro-element to simulate dynamic soil-structure interaction. *Eng Struct*. 2009;31(12):3034-3046. doi:10.1016/j.engstruct.2009.08.007
87. Pisanò F, Flessati L, di Prisco C. A macroelement framework for shallow foundations including changes in configuration. *Geotechnique*. 2016;66(11):910-926. doi:10.1680/jgeot.16.P.014
88. di Prisco C, Flessati L, Frigerio G, Lunardi P. A numerical exercise for the definition under undrained conditions of the deep tunnel front characteristic curve. *Acta Geotech*. 2018;13(3):635-649. doi:10.1007/s11440-017-0564-y

89. Di Prisco C, Vecchiotti M. A rheological model for the description of boulder impacts on granular strata. *Géotechnique*. 2006;56(7):469-482. doi:10.1680/geot.56.7.469
90. Flessati L, di Prisco C, Callea F. Numerical and theoretical analyses of settlements of strip shallow foundations on normally consolidated clays under partially drained conditions. *Geotechnique*. 2021;71(12):1114-1134. doi:10.1680/jgeot.19.P.348
91. di Prisco C, Flessati L, Porta D. Deep tunnel fronts in cohesive soils under undrained conditions: a displacement-based approach for the design of fibreglass reinforcements. *Acta Geotech*. 2020;15(4):1013-1030. doi:10.1007/s11440-019-00840-8
92. di Prisco C, Pisanò F. An exercise on slope stability and perfect elastoplasticity. *Géotechnique*. 2011;61(11):923-934. doi:10.1680/geot.9.P.040
93. Drescher A, Detournay E. Limit load in translational failure mechanisms for associative and non-associative materials. *Geotechnique*. 1993;43(3):443-456. doi:10.1680/geot.1993.43.3.443
94. Vermeer PA. The orientation of shear bands in biaxial tests. *Géotechnique*. 1990;40(2):223-236. doi:10.1680/geot.1990.40.2.223
95. Van Eekelen SJM, Bezuijen A, Alexiew D, The Kyoto Road piled embankment: 31/2 years of measurements. In: *9th International Conference on Geosynthetics - Geosynthetics: Advanced Solutions for a Challenging World, ICG 2010*, 2010, pp. 1941-1944.
96. Guido VA, Knueppel JD, MA S, Plate loading tests on geogrid-reinforced earth slabs; 1987.
97. Abusharar SW, Zheng JJ, Chen BG, Yin JH. A simplified method for analysis of a piled embankment reinforced with geosynthetics. *Geotext Geomembranes*. 2009;27(1):39-52. doi:10.1016/j.geotexmem.2008.05.002
98. Lu W, Miao L. A simplified 2-D evaluation method of the arching effect for geosynthetic-reinforced and pile-supported embankments. *Comput Geotech*. 2015;65:97-103. doi:10.1016/j.compgeo.2014.11.014

How to cite this article: Mangraviti V, Flessati L, di Prisco C. Mathematical modelling of the mechanical response of geosynthetic-reinforced and pile-supported embankments. *Int J Numer Anal Methods Geomech*. 2023;1-29. https://doi.org/10.1002/nag.3586

APPENDIX A

As was mentioned in Section 2.2, in subdomain 4 of Figure 8 the arching mechanism takes place and the stresses/strains are not uniform. Nevertheless, in case of CPS embankments, this does not significantly influence the displacement field at both top and bottom of subdomain 4 (dashed line of Figure A1). This is almost uniform and practically coincident with its average value and justifies the assumption of reproducing the response of subdomain 4 as a one-dimensional non-linear spring.[40]

On the contrary, in case of GRPS embankments, the displacement field differs from the average one (solid line of Figure A1). Nevertheless, in agreement with the introduced substructuring approach, average stresses and displacements are used in the constitutive model to both describe subdomain 4 response and define the transferring function (Equation 19) governing the membrane mechanical response. As is shown in Sections 4 and 5, this simplifying assumption does not compromise the capability of the model of reproducing the numerical results and field measurements.

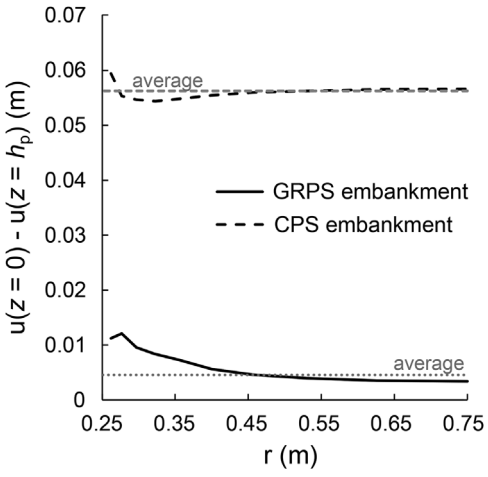

FIGURE A1 Net settlements of subdomain 4 along *r*.

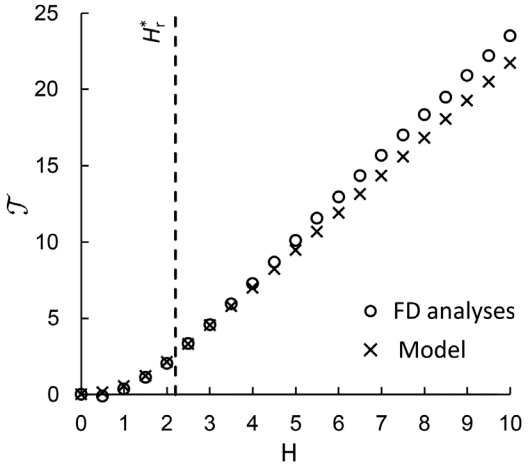

FIGURE A2 Non-dimensional force transmitted by the plastic slider for the reference case by Mangraviti et al.[35]

APPENDIX B

As for the case of CPS embankments,[40] also for GRPS embankments model, a Mohr-Coulomb failure condition is assumed for the plastic slider (element E in Figure 11):

$$\dot{\mathcal{T}} = \dot{\mathcal{N}} \, tan\phi'_{ss}, \tag{A1}$$

being $\dot{\mathcal{T}}$ and $\dot{\mathcal{N}}$ the increments of non-dimensional tangential and normal forces transferred throughout the process zone, respectively. To calculate $\mathcal{N}$, a geostatic distribution of vertical stress is assumed for $0 < z < h_p$:

$$\mathcal{N} = \frac{\int_0^{h_p} \pi\gamma\,(h-z)\,\bar{k}ddz}{\gamma d^3} = \pi\bar{k}HH_p - \pi\bar{k}\frac{H_p^2}{2}. \tag{A2}$$

Therefore, its increment is:

$$\dot{\mathcal{N}} = \pi\bar{k}H_p\dot{H} + \pi\bar{k}\left(H - H_p\right)\dot{H}_p. \tag{A3}$$

By assuming such a mechanical behaviour, the agreement of the model predictions and FD numerical results, in terms of evolution of $\mathcal{T}$ with H (Figure A2) is very satisfactory.

APPENDIX C

The compliances of the elastic springs C and D of Figure 11 are, by definition, equal to:

$$C_1^{irr} = C_2^{irr} = \frac{H_p}{E_{oed,e}}\frac{E_{oed,f}}{L}, \tag{A4}$$

$$C_3^{irr} = \frac{H - H_p}{E_{oed,e}}\frac{E_{oed,f}}{L}. \tag{A5}$$

To calculate C_{diff} and C_{av} (Equations 14 and 15) the same theoretical procedure followed for CPS embankments, is used also for GRPS embankments. In particular:

a. the non-dimensional force transferred by the plastic slider (Equations A1 and A3) is introduced in the balance of momentum along the vertical direction:

$$\dot{\Sigma}_c = \dot{H} + \frac{4\dot{\mathcal{T}}}{\pi} = \left(1 + 4\bar{k}tan\phi'_{ss}H_p\right)\dot{H} \tag{A6}$$

$$\dot{\Sigma}_f = \dot{H} - \frac{4\dot{\tau}}{\pi\left(S^2-1\right)} = \left(1 - \frac{4\bar{k}tan\phi'_{ss}H_p}{S^2-1}\right)\dot{H} \tag{A7}$$

being

$$\Sigma_c = \frac{\sigma_c}{\gamma d} \tag{A8}$$

and

$$\sigma_c = \frac{\int_0^{2\pi}\int_0^{d/2}\sigma_v(r)\,r\,d\vartheta\,dr}{\pi d^2/4} \tag{A9}$$

b. Equations (A6) and (A7) are introduced in the compatibility conditions along the vertical direction and in the spring constitutive relationships:

$$\dot{U}_{t,c} = C_1^{irr}\dot{\Sigma}_c + C_3^{irr}\dot{H} = \left[C_1^{irr}\left(1 + 4\bar{k}\tan\phi'_{ss}H_p\right) + C_3^{irr}\right]\dot{H} \tag{A10}$$

$$\dot{U}_{t,f} = \left(C_2^r\left(U_{b,f}\right) + C_2^{irr}\right)\dot{\Sigma}_f + C_3^{irr}\dot{H} = \left[\left(C_2^r\left(U_{b,f}\right) + C_2^{irr}\right)\left(1 - \frac{4\bar{k}\tan\phi'_{ss}H_p}{S^2-1}\right) + C_3^{irr}\right]\dot{H} \tag{A11}$$

c. Equations (A10) and (A11) are introduced in the definitions of $\dot{U}_{t,diff}$ and $\dot{U}_{t,av}$ (Equations 8 and 9):

$$\dot{U}_{t,diff} = \left\{C_2^r\left(U_{b,f}\right) + C_2^{irr} - C_1^{irr} - 4\bar{k}\tan\phi'_{ss}\left[C_1^{irr} + \frac{C_2^r\left(U_{b,f}\right) + C_2^{irr}}{\left(S^2-1\right)}\right]H_p\right\}\dot{H} = C_{diff}\dot{H} \tag{A12}$$

$$\dot{U}_{t,av} = \left[\frac{C_1^{irr}}{S^2} + \frac{\left[C_2^r\left(U_{b,f}\right) + C_2^{irr}\right]\left(S^2-1\right)}{S^2} - \frac{4\bar{k}\tan\phi'_{ss}H_p\left[C_2^r\left(U_{b,f}\right) + C_2^{irr} - C_1^{irr}\right]}{S^2} + C_3^{irr}\right]\dot{H} = C_{av}\dot{H} \tag{A13}$$

APPENDIX D

In Figure A3 the numerical results from a parametric study are compared with the results obtained by using Equation (19) in which $\alpha = 250$. In particular, in Figure A3(A,B) different mechanical properties for the reinforced foundation soil (J and $E_{\mathrm{oed,f}}$) are considered, whereas in Figure A3(C–E) different geometries (s, d, l, in Figure A3(C–E), respectively) are accounted for. For all the cases considered, the agreement is satisfactory.

Analogously, the results obtained by imposing $\beta = 24$ into Equation (27) are compared with the numerical results of a parametric study in Figure A4. In particular, in Figure A4(A,B) different mechanical properties (J and E_{oedf}) are considered, whereas in Figure A4(C–E) different geometries (s, d, l, in Figure A4(C–E), respectively) are accounted for. Even in this case the agreement is satisfactory.

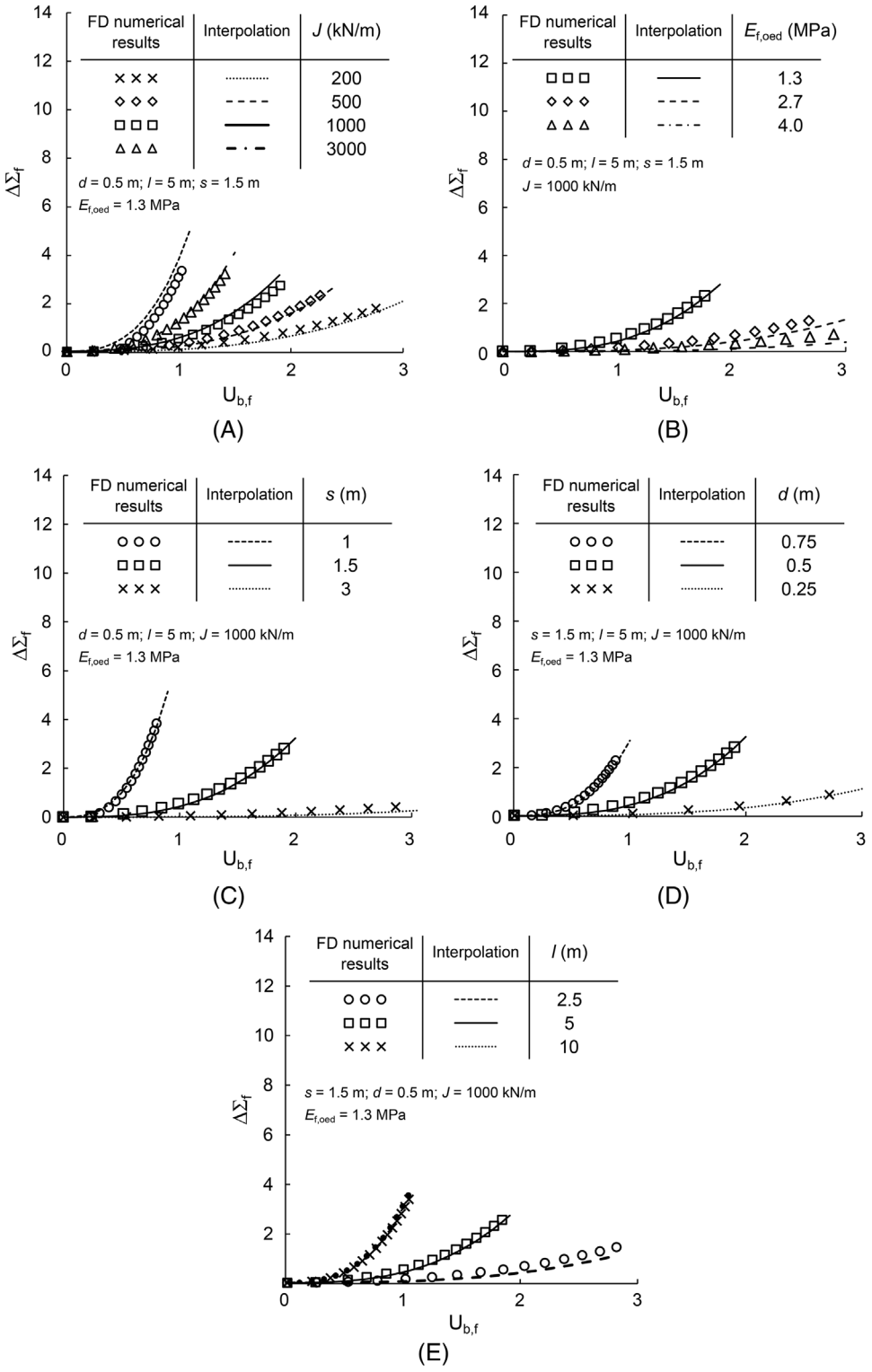

FIGURE A3 Comparison of FD numerical results against interpolation in terms of non-dimensional average stress applied on the membrane and non-dimensional settlements of the membrane by changing: (A) membrane axial stiffness; (B) foundation soil oedometric stiffness; pile (C) spacing; (D) diameter and (E) length.

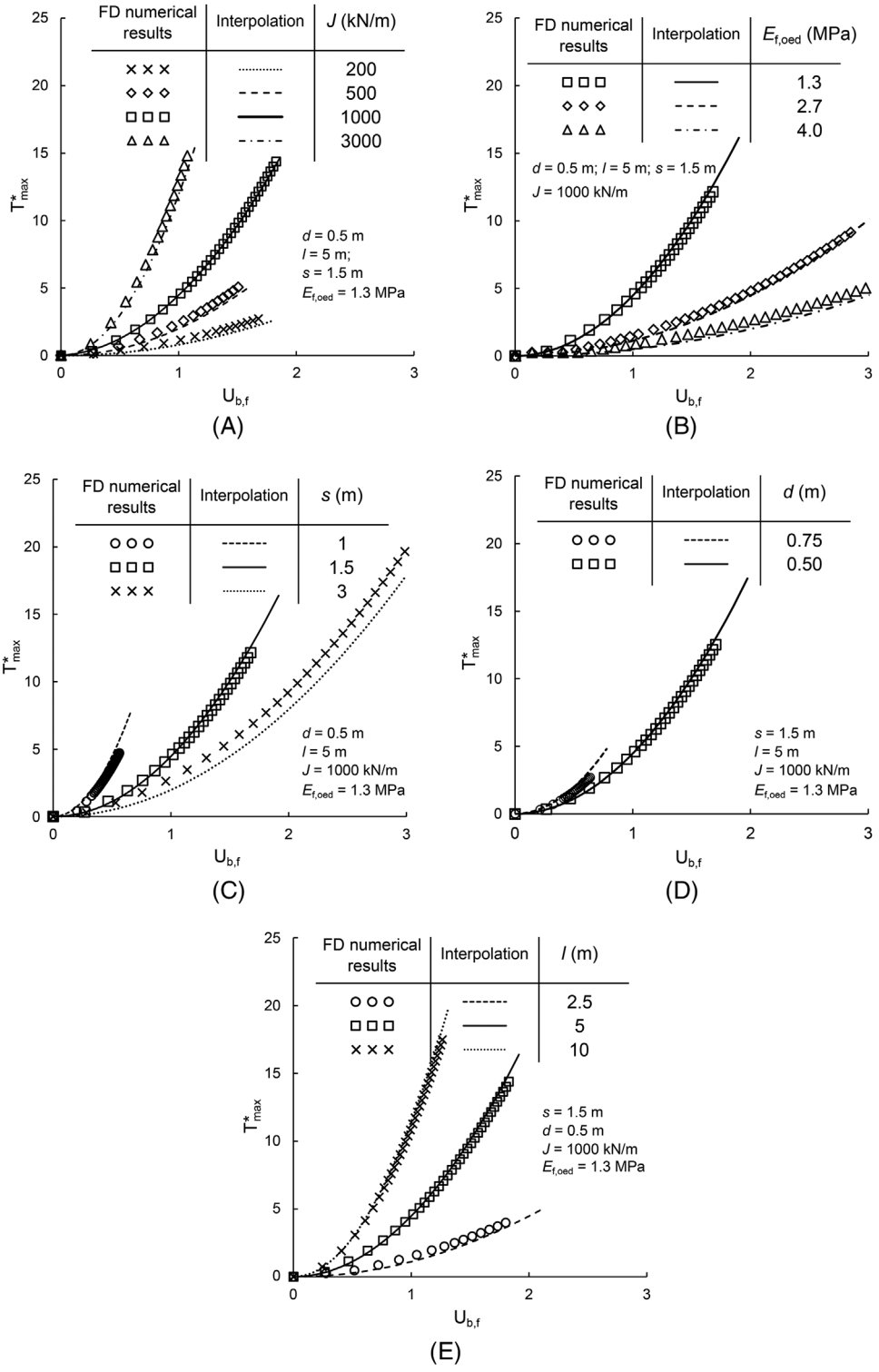

FIGURE A4 Comparison of FD numerical results against interpolation in terms of non-dimensional average stress applied on the membrane and non-dimensional settlements of the membrane by changing: (A) membrane axial stiffness; (B) foundation soil oedometric stiffness and pile (C) spacing, (D) diameter and (E) length.